Stable heat and particle flux detachment with efficient particle exhaust in the island divertor of Wendelstein 7-X

Oliver Schmitz[1], Y. Feng[2], M. Jakubowski[2], R. König[2], M. Krychowiak[2], M. Otte[2], F. Reimold[2], T. Barbui[1,3], C. Biedermann[2], S. Bozhenkov[2], S. Brezinsek[4], B. Buttenschön[2], K.J. Brunner[2], P. Drewelow[2], F. Effenberg[1,3], E. Flom[1], H. Frerichs[1], O. Ford[2], G. Fuchert[2], Y. Gao[2,4], D. Gradic[2], O. Grulke[2], K. C. Hammond[2,3], U. Hergenhahn[2], U. Höfel[2], J. Knauer[2], P. Kornejew[2], T. Kremeyer[1,2], H. Niemann[2], E. Pasch[2], A. Pavone[2], V. Perseo[2], L. Rudischhauser[2], G. Schlisio[2], T. Sunn Pedersen[2], U. Wenzel[2], V. Winters[1,2], G.A. Wurden[6], D. Zhang[2] and the W7-X team

1 - University of Wisconsin - Madison, Department of Engineering Physics, WI, USA
2 - Max Planck Institute for Plasma Physics, Greifswald, Germany
3 - Princeton Plasma Physics Laboratory, Princeton, NJ, USA
4 - Inst. of Energy- and Climate Research, FZ Jülich, Jülich, Germany
5 - Auburn University, Auburn, USA
6 - Los Alamos National Laboratory, Los Alamos, USA

E-mail: `oschmitz@wisc.edu`

Abstract.

The island divertor concept is an innovative and promising idea to handle heat and particle exhaust in stellarators. At the Wendelstein 7-X (W7-X) stellarator, this divertor concept plays a central role in the device mission to demonstrate reactor relevant plasma confinement for steady-state time scales of up to 30 minutes in the high-performance campaign (OP2) starting in 2022. During the recently concluded first campaign with the inertially cooled island divertor, a large step in the experimental qualification of this divertor concept has been made. In discharges heated with Electron Cyclotron Resonance Heating of $5-6$ MW, central densities in the range of $0.7-1.2\times10^{20}$ m^{-3} have been reached in combination with full divertor heat flux detachment. Also, significant neutral gas pressures and neutral compression ratios were shown for the first time in combination with reduced divertor particle flux. The divertor heat loads drop by an order of magnitude from > 5 MW m^{-2} to below 0.5 MW m^{-2} with increasing density, and substantial compression of neutrals reaching neutral pressure in the sub-divertor volume of $> 6.0\times10^{-4}$ mbar was seen. These elevated neutral pressure levels can be obtained and maintained with an up to 80% reduction of the particle fluxes onto the divertor target tiles. This discharge scenario was held stably detached for up to 28 seconds, which is equivalent to several hundred energy confinement times τ_E and longer than the time scales for current relaxation. No impurity accumulation was seen at constant $Z_{eff} \approx 1.5$ and the stored energy stayed constant at levels of $W_{dia} > 600$ kJ. The level of neutral pressure and compression reached in this scenario extrapolates well to the steady-state particle exhaust requirements for high-performance steady-state operation in OP2, in which the fully actively cooled High-Heat-Flux divertor will be available. An overview of this recently discovered divertor regime is given and the status of the physics understanding based on modeling of these regimes with the EMC3-EIRENE code is presented.

Keywords: Stellarator, Island Divertor, Plasma Edge Physics and Material Interaction

Submitted to: *Nucl. Fusion*

1. Introduction of the island divertor concept

Stellarators are inherently capable of stationary confinement of high temperature plasmas as they do not require external current drive [1, 2, 3]. The confining magnetic field, including the necessary rotational transform, is produced by external coils. This intrinsic steady state capacity, however, puts the quest for an appropriate plasma material interface design and a reliable heat and particle exhaust concept that can handle the heat and particle fluxes in a stellarator in a steady state fashion, at highest priority [4, 5, 6]. Because stellarator optimization [7, 8] for low neoclassical transport, reduced energetic particle losses and stable plasma equilibrium properties can be obtained in various magnetic configurations, the divertor design depends on the actual choice of the equilibrium of the plasma core domain. Various choices are known [5] on how to constrain the plasma boundary by placing material surfaces around the three-dimensional stellarator equilibrium in a way that minimizes consumption of vacuum volume and optimizes for efficient heat and particle exhaust and sufficient neutral pumping to maintain stable plasma density and impurity conditions.

One candidate divertor concept for stellarators and heliotrons is the helical divertor as implemented in the Large Helical Device (LHD) [9, 10]. The helical field line trajectories departing from the stochastic domain that surrounds the LHD plasmas are intersected in helical divertor slots, which recently also have been equipped with active pumping [11] establishing a low recycling regime with full control of the divertor neutral particle source [12, 13]. Another concept is the non-resonant divertor [14], in which no low order rational surface is required to form the magnetic field structure of the divertor. Instead, field lines departing from sharp corners of the magnetic equilibrium intersect the divertor targets. This can make the divertor structure insensitive to internal plasma equilibrium changes. This stellarator divertor concept was explored by field line tracing in form of helical troughs first for W7-X [15] and then for devices with quasi-symmetric optimization like the Helically Symmetric Experiment (HSX) [16, 17]. No experimental verification of the high-β features of the non-resonant divertor have been performed beyond basic divertor characterizations at HSX [18]. However, both the helical as well as the non-resonant divertor feature a resiliency against plasma equilibrium changes due to internal plasma currents and even shifts of the magnetic axis. In Wendelstein 7-X [5, 15, 19, 20] as well as its predecessor Wendelstein 7-AS [21, 22], a low order rational surface in the plasma edge enables the utilization of a magnetic island structure as the interface to plasma facing components in the Island Divertor. This approach can be more sensitive to internal plasma currents that affect the position of the low order rational surface in the plasma edge and hence the magnetic structure of the island divertor [23]. The magnetic island volume represents a separated plasma domain which can be optimized to match the requirements for heat dissipation, neutral compression, and impurity screening [20].

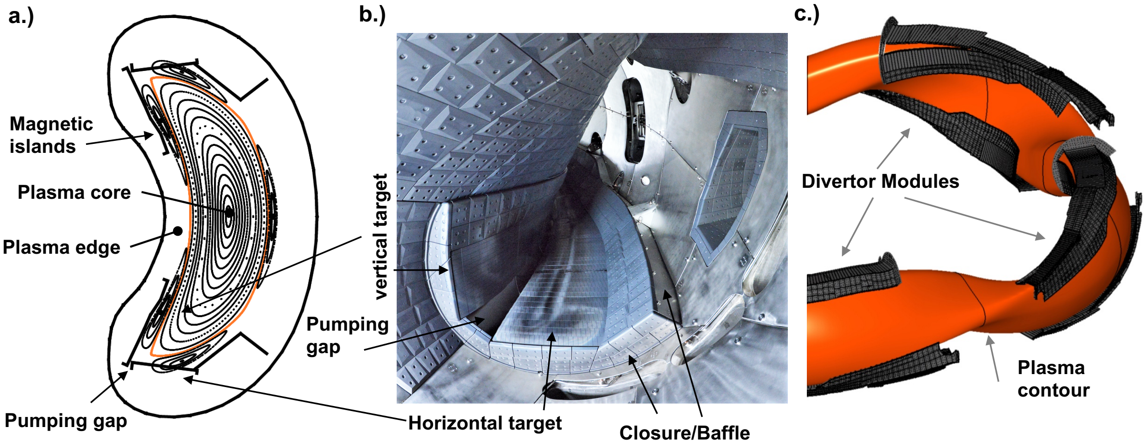

Figure 1: The island divertor at Wendelstein 7-X: (a) the magnetic structure as Poincaré plot visualizing the five magnetic islands for the $n/m = 5/5$ standard magnetic configuration and the good magnetic flux surfaces in the plasma core, (b) a photo of the vessel interior and of one divertor module is shown, taken after the 2018 divertor campaign and (c) the plasma contour with six out of ten divertor modules is depicted.

The general layout of the island divertor concept and its actual implementation in the W7-X device is shown in figure 1. The design considerations and choices made for this divertor implementation are discussed in [24, 25] from a historic perspective, in [5] as part of the international stellarator divertor program and in [26] in view of first results. As described in [24, 25], the guiding principles encompass that divertor targets with a large enough surface need to be implemented in the 3D device design to spread the heat flux sufficiently. This includes a shallow incident angle for magnetic spreading of the heat flux. The divertor needs to feature an opening - the pumping gap - that is arranged such that neutrals can enter the pumping domain and can be exhausted. This requires a close proximity of the strike line on the target plate to the pumping gap to foster neutral collection. The analysis of the particle balance and recycling characteristics of the island divertor described in [27, 28, 29] showed that stable density control can be expected. Also, the magnetic variability in the magnetic island width and strike line position enabled by the divertor control coils was shown to be a versatile actuator for control of the recycling and pumping features [27]. In essence, the island provides a buffer volume between the divertor target plates and the core plasma. The properties of this buffer plasma determine the divertor functionality. Low temperatures and high plasma densities are predicted to provide an effective collection channel for exhausted main species gas with a high retention probability for recycled neutrals. The position of the strike line with respect to the pumping gap controls how many neutrals can be collected in the pumping domain. The closer the strike line, the higher the collection probability. The island width w_{isl} can be used to control the width of the buffer plasma as well as the magnetic connection length L_c which provides means to regulate the parallel to perpendicular transport ratio. This impacts the deposition profiles on the divertor targets as well as the parallel flow profiles in the momentum balance [29]. The eventual island divertor implementation for W7-X is the result of these divertor design considerations and optimizations which were performed in the framework of the overall optimization of the magnetic configuration for its core plasma confinement and stability properties. The role of these physics principles for detached scenarios is analyzed in [20] and will be referred to extensively in this paper.

In figure 1.a, the magnetic structure of the plasma equilibrium is shown at the bean shaped cross section in form of a Poincaré plot. The plasma core with good flux surfaces is seen followed radially outward by a domain with five substantially sized magnetic islands. They form the plasma boundary domain and are intersected by divertor target plates forming the island divertor unit. The target plates are comprised out of a vertical target and a horizontal target, as shown in the picture of figure 1.b. The horizontal and vertical target plate, together with a baffle on top of both targets and the divertor closure form one divertor module. In between these target plates, the divertor pumping gap is located. There are ten of these modules, two per device segment in the five fold symmetry setup of W7-X. The divertor modules are aligned with the plasma equilibrium as close fitting units shown in figure 1.c. The domain in between the horizontal and vertical target is open towards the divertor housing, which enables collection of neutrals and the build up of neutral pressure for pumping.

The island divertor was operated with the inertially cooled Test Divertor Unit (TDU) in 2017/18. Promising results were obtained suggesting the island divertor concept as a possible way to establish a reliable plasma wall interface with minimal control needs [26, 30, 31]. In this paper, we show for the first time a stably detached efficient heat and particle exhaust regime in the island divertor, in which the heat fluxes to the divertor surfaces vanish and particle fluxes are reduced by up to 80%. At the same time sufficient neutral pressure for efficient particle exhaust is obtained. It is found to be compatible with the required steady state particle exhaust for the upcoming steady state campaigns in 2022 and beyond. At this point, the fully water cooled High Heat Flux (HHF) divertor that includes the sub-divertor cryogenic pumping system will have been installed. The plasma discharges discussed in this paper are heated by electron cyclotron resonance heating (ECRH) in second harmonic extraordinary (X2) or ordinary (O2) mode for high density absorption [32].

To provide experimental information on the features of the SOL and divertor plasma at W7-X during the detachment experiments, we will use in this paper in particular the following quantities. Their according relevance for the divertor functionality as a system component for steady state plasma operation for the upcoming HHF divertor campaign is pointed out. We here also conceptually link to the divertor requirements for a stellarator reactor [33] in a general sense:

- divertor heat and particle fluxes: these are the key figures of merit for a detached divertor and need to be reduced enough to maintain the divertor integrity. A typical value for the maximal heat flux density for actively water cooled solid state plasma facing components is 10 MW m^{-2} [34]. The according number for a reactor system will depend on the actual choice of plasma facing components, i.e. liquid or solid and the cooling technology. The High-Heat-Flux divertor at W7-X is designed to handle this heat flux [25], but in the experiments considered here, this value is barely reached due to the relatively low heating power density at $P_H = 6$ MW that was available. Therefore, the investigation of the heat flux reduction will be performed in reference to the maximal heat flux density reached for a given plasma scenario during the attached phase of the discharge.
- neutral pressure in the divertor: only if sufficient neutral pressure is maintained inside of the divertor pumping volume while detaching the particle fluxes, exhaust of main species and impurity particles can be provided. In a stellarator reactor the pumping capability will need to be sufficient to exhaust excess fuel gas as well as the helium ash [35]. In this paper, we discuss results related to exhaust of excess fuel and hydro-carbon impurities to maintain stable density conditions at compatible impurity concentrations. The exhaust of helium is not studied.
- neutral compression: this metric denotes the ratio of the downstream neutral pressures to the upstream values; this ratio should be as high as possible to show that neutrals are collected in the divertor for optimum access to the pumping system. Also, the neutral density in the main chamber, i.e. upstream, need to be small to avoid charge-exchange acceleration of neutrals that can (a) cause first wall sputtering and (b) build-up a fast neutral source for a high level of upstream fueling that can make the density control challenging.
- radiative fraction: this is the ratio of radiated power to the input power and it should be high with most of it being located in the island divertor and scrape-off layer domain. Adverse impact of high radiation on the core plasma parameters should hence be minimized. For a reactor, such a scenario with dominant plasma

edge and SOL radiation has to be generated in a stable fashion [33].

- core plasma parameters: the plasma core needs to be stable during the transition into detachment so that the necessary performance can be maintained. For a stellarator reactor, the plasma core performance needs to be sufficient to maintain plasma burn or ignition [33]. For W7-X, we will use the best performance of the plasma discharge used for the detachment study as reference to investigate any possible performance degradation. This is typically the attached phase of the discharge which precedes the density ramp up yielding detachment.

The trends of these parameters with increasing density when approaching detachment depend on specifics of the magnetic structure, physical implementation, and material of the island divertor. Three specific elements are of importance: First, the size of the magnetic island, as well as the location of the strike line with respect to the pumping gap of the divertor, is an important actuator that can be controlled externally by the planar coils and the divertor control coils. The closer the strike line and hence the dominant recycling domain is located to the pump gap, the more likely it is to collect the neutrals produced by the recycling process. It will be shown that the divertor scenarios possible at W7-X in the standard divertor configuration allow to change the width of the island which comes with a change of the position of the strike line. Second, the divertor baffling in the 3D geometry is complex. Optimal closure was obtained by installing a full baffle with front and end closures of the divertor pumping domain [36]. However, unavoidable gaps in the closure result in a neutral leakage that is expected to range between $5 - 30\%$ of the neutral particles collected in the pumping domain. This divertor leakage can diminish the pumping capability of the divertor and yield loss of density control if too many neutrals are available for fueling of the core plasma outside of the divertor. Third, the divertor targets are made out of Carbon (Carbon Fiber Composite CFC) which introduces an intrinsic impurity source that is linked to the incoming ion flux in a given scenario due to sputtering. Therefore, the particle flux in the divertor is linked to the impurity amount available in the divertor for radiation and hence to the energy dissipation from radiation. The role of all three aspects will be discussed with respect to the experimental observations in this paper.

The paper is organized as follows. In section 2, specific aspects of the magnetic field structure in the SOL of W7-X and ITER as a tokamak reference are discussed to relate the observations and our interpretation of this first assessment of detachment in the island divertor to the well studied detachment process in tokamak divertors. In section 3, the thermal detachment properties are described followed by a discussion of the reduced particle fluxes and simultaneous build up of significant neutral pressures in section 4. The role of radiative power losses from the plasma edge due to impurity radiation is discussed in section 5. In section 6, the steady state properties of this regime are discussed and the paper is concluded by a summary and discussion in the final section 7.

2. Magnetic topology considerations to discuss island divertor detachment with a basic connection to tokamak detachment in a single-null divertor

Detachment is the process of reduced heat and particle fluxes to the divertor targets in order to maintain heat fluxes within technical limitations of the material and cooling capacity. Also, particle fluxes need to be reduced to keep erosion and impurity production on tolerable levels in regards of both the device impurity content as well as to maintain the integrity of the plasma facing components. In addition, the particle flux contributes to the power and momentum balance at the targets [20, 37, 38, 39], that defines the relation between upstream, i.e. in the main chamber in the volume of the device mid-plane and downstream plasma pressures to maintain high upstream pressure [40]. The incoming ion flux also contributes to the deposited energy flux onto the divertor targets when recombining to neutral particles in the material [41, 42]. The resulting requirement of reduced particle flux then needs to be combined with maintaining of high enough divertor neutral pressure for sufficient pumping. These functional requirement of reduced divertor loads combined with sufficient neutral pressure will guide the presentation of experimental results in this paper.

To understand the physical processes of detachment, specific models have been developed during several decades of exploring this process in the tokamak configuration. The simple and complex-SOL approaches and the two-point model as introduced for instance in [43], [44] and [45] are the most basic approaches that are regularly used to cope with the complex, non-linear process of divertor detachment in tokamaks. Many papers and reviews exist that elaborate on the detachment process (see for instance [38, 39, 46]) as well as the projection towards ITER [34, 47]. Also, a comprehensive discussion about the similarities and differences between this tokamak basis and the stellarator and heliotron divertor physics can be found in [48] and [49].

In order to aid the understanding of the first of its kind experimental observations for the island divertor that are presented in this paper, in reference to canonical tokamak analysis approaches, we provide a brief argument in terms of the magnetic field structure of the plasma edge that will allow to present the measurements discussed in terms of upstream, i.e. in the vicinity of the last closed flux surface in the main chamber, and downstream, i.e. at the divertor target plates, conditions. It is important to note that the results presented in this paper are the first observations of physical quantities in this complex SOL physics process. We will survey the results in a consistent manner, but the detailed physics understanding is still emerging and will be expanded in future experimental campaigns. Hence, much of the detailed physics discussions of the specifics of the detachment process in the island divertor and detailed comparisons to the process in the tokamak configuration is deferred to future papers.

In tokamaks, the relation between the core plasma, the divertor plasma, and plasma material interface is quantified by comparing upstream measurements in the vicinity of the last closed flux surface (LCFS) with downstream parameters at the divertor target. This is motivated by the physics underlying detachment. Heat and particle influx into the open field line SOL domain are transported along the field lines towards the end point on the targets. The exact features of the parallel transport governs the downstream profiles and the magnitude of the arriving fluxes. See, for instance, the two-point model as described in [45] or following [39] as a recent review. A particle, power, and momentum balance is established between the upstream and downstream position. In the attached regime, convective heat, and particle fluxes, and the associated momentum flux governs this equilibrium. When the density is increased, the downstream density starts to rise faster than the upstream density and a regime of high-recycling is entered. In this regime, ionization as well as radiation power losses in the divertor volume cause energy dissipation and reduced upstream particle sources as well as friction between plasma and neutral gas along the field line can cause momentum losses. These mechanisms eventually reduce the heat flux to the divertor and also the particle flux. In this paper, a first systematic overview of the properties of the island divertor plasma and its coupling to the main plasma in the confined, domain during the transition into detachment and for long detached phases, is presented.

To approach an analysis of the island divertor features when detachment is achieved, we need to sort the available measurements into the up-/downstream scenario presented before. To do this, the magnetic connection length L_c is an important quantity as it defines the geometrical scale length for the parallel transport. Therefore, the magnetic field structure in the plasma edge is important to understand the link between tokamaks and stellarators. In figure 2, a comparison of the SOL magnetic field structure is shown for W7-X (figure 2.a) and ITER (figure 2.b). For each device, a plot of the equilibrium surfaces is shown. For ITER, one single field line at $\Delta r = 1$ cm outside of the last-closed flux surface is traced towards both end point on the inner and outer divertor, respectively. The equilibrium shown is located at the upstream position, i.e. the toroidal location where this field line intersects the poloidal plane at the outer mid-plane position. For W7-X, one field line is marked that connects one upper divertor with one lower divertor module. Equilibrium surface plots are shown at the toroidal position of these divertor modules and at the toroidal positions that lay toroidally in between. At these positions, the island flux tube intersects these equilibria at the radially inside and outside mid-plane position. Another field line is shown that is started at $\Delta s_{target} = 1$ cm above the upper divertor target surface to show the precession of these SOL field lines around the torus for many turns. Details of the complex connection length L_c structure for this stellarator configuration are discussed later. It is important to note that the magnetic field lines stay within one magnetic island and hence, five such magnetic SOL flux bundles form the island divertor SOL at W7-X.

For the ITER case, the outer mid-plane is marked that is often used as the upstream

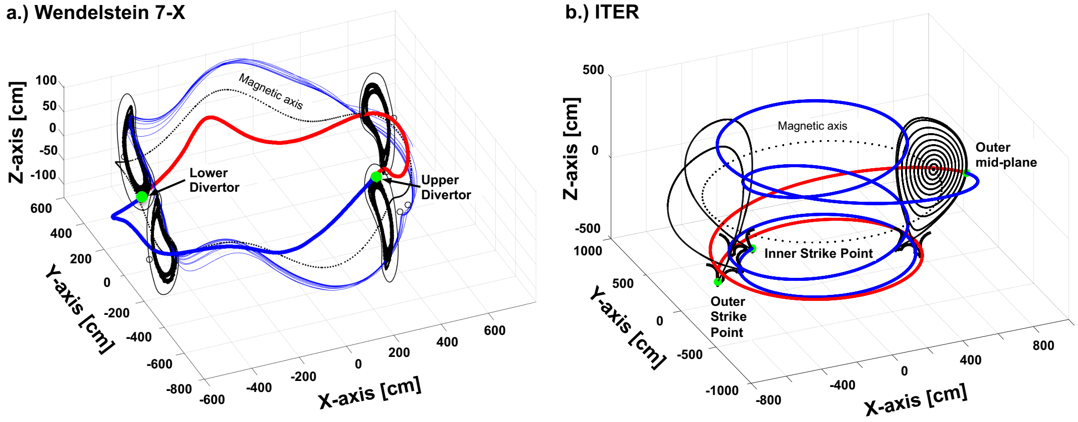

Figure 2: Comparison of the magnetic field structure in the scrape-off layer (SOL) of Wendelstein 7-X (figure part a) and ITER (figure part b). For each device, a plot of the equilibrium surfaces is shown. For ITER, one single field line at $\Delta r = 1$ cm outside of the last-closed flux surface is traced towards both end points on the inner (marked in blue) and outer divertor (marked in red), respectively. The equilibrium shown is located at the upstream position, i.e. the toroidal location where this field line intersects the poloidal plane at the outer mid-plane position. For W7-X, one field line is marked that connects one upper divertor with one lower divertor module. The first part, i.e. upper to lower divertor is marked in red and the second part, i.e. from the lower to the upper divertor. Equilibrium surface plots are shown at the toroidal position of these divertor modules and at the toroidal positions that lay toroidally in between. At these positions, the island flux tube intersects these equilibria at the radially inside and outside mid-plane position. Another field line is shown that is started at $\Delta s_{target} = 1$ cm above the upper divertor target surface to show the precession of these SOL field lines around the torus for many turns. Details of the complex connection length structure are discussed in the text.

position to relate core plasma parameters to the divertor conditions. One field line representative for a magnetic flux tube was traced from this upstream position into the downstream intersection point in the inner (blue part of the field line) and outer (red part of the field line) divertor. The helicity of the field line that establishes the connection between the upstream and downstream position to discuss detachment is obvious. The comparable types of field lines for the W7-X configuration shown in figure 2.a shows the low shear of the magnetic field in W7-X. The blue/red colored field line shows a field line that was started right on the divertor target of one of the five upper divertor modules and connects to the $\varphi = 180^o$ distant lower divertor module. The red field line indicates the first part of this trace, the blue field line the second part, i.e. a field line that was started at the intersection point and traced forward until it hits the upper divertor again. This structure shows the connected divertor feature of the $n/m = 5/5$ standard divertor configuration that we address in this paper. Five of these connected flux tubes from one upper to one lower divertor exist. The experimental results discussed in this paper will hence be presented in alignement with one of these five SOL flux tubes that are formed by one of the five magnetic islands shown in figure 1.a.

If we now start a field line at some distance away from the divertor target, it can be seen that we place this starting point inside of this magnetic island structure that connects this pair of upper/lower divertor modules. Therefore, field lines will stay inside of this flux tube but precess around the torus for a significant amount of toroidal turns, which yields large connection length L_c of several hundred meters. This is often referred to as an advantage of stellarators, because during this long precession perpendicular transport can flatten the radial plasma profiles and hence cause more shallow heat and particle flux profiles with reduced peak heat fluxes on the island divertor target surfaces [20, 48, 49]. Such a field line - started traced within another of the five SOL flux tubes for better visibility - is shown as a thin blue line in figure 2.a for W7-X. This field line goes around the torus six times before intersecting the target and hence features a much longer value of L_c than the short field line discussed as example before. The reason for this slow poloidal precession of the field line on the flux surfaces inside of the island is the low internal magnetic shear inside of the island [20, 49].

These features point out that the magnetic field structure of the W7-X configuration discussed in this paper is more complex than the tokamak situation. However, it is important to note that one upper divertor module is connected in this configuration by a magnetic island with a lower divertor module $\varphi \approx 180^o$ apart. This establishes an edge magnetic field structure in which an upstream and downstream position can be identified. In fact, one will need to discuss two upstream positions, as the field line makes a full toroidal turn and we find one intersection at the intermediate symmetric planes that intersects the poloidal plane at the inside of the torus (red field line) and one at the outside (blue field line). The details of the distribution of $L_c(R, Z)$ across the magnetic island will be discussed in the next section and will aid to discuss the location of the experimental measurements that are utilized.

3. Observation of thermal detachment in the island divertor

A characteristic measure for the heat flux loading of a divertor in any magnetic confinement fusion device is the scaling of the heat flux with plasma density [38, 47, 50, 51, 52]. This relationship is important, as with approaching high plasma core density for optimizing the fusion gain, the divertor heat fluxes need to stay within technical limits of the divertor surface material. For instance, melting has to be avoided and material erosion needs to be kept low. Also, cooling and thermal cycling limits need to be accommodated to maintain the integrity of the plasma wall interface and also of the structural and cooling components of the divertor unit. In figure 3, an overview of the heat flux characteristic during a density ramp from $n_{e,l.i.} = 9.5 - 11.5 \times 10^{19}$ m^{-2} in line integrated density $n_{e,l.i.}$ along a plasma path segment with length $l_{l.i.} = 1.3$ m is shown [53]. The discharge scenario (W7-X reference program 20180814.024) considered here and throughout the paper is the Standard Divertor Configuration (SDC) with a $\iota = n/m = 5/5$ poloidal (m) and toroidal (n) mode number configuration at a heating power of $P_{ECRH} = 6MW$. The ECRH heating was supplied in these experiments by X2 mode heating for densities up to $n_{e,l.i.} = 6.0 \times 10^{19}$ m^{-2} after which the ECRH system was switched to O2 heating. The density range utilized in these experiments was a result of fairly high start density of $n_{e,l.i.} = 9.0 \times 10^{19}$m^{-2} for these heating powers. As discussed later based on results of gas balances, particles desorbed from the wall reservoir yielded this density naturally and reliably. However, the wall reservoir for these discharges also prevented access to lower densities for the detachment studies presented here. Therefore, complete scans of the recycling flux from attached into high recycling and finally detached condition are not available. From this natural startup density level on, a small density increase was sufficient to obtain the detached plasma regime discussed. Establishing this working point was reliably obtained throughout the campaign and did not depend on the time after the boronization. During the 2018 campaign with the Test Divertor Unit (TDU), three boronization were performed [26, 54]. The promising divertor regime was seen after boronization of the vacuum vessel was started. A central element in this advance of the divertor regime after boronization was that the Oxygen content was reduced. This reduced the impurity concentration around the plasma and hence reduced the radiated power losses which then allowed to reach higher densities at the available heating power levels [31]. Please see [54] for details of the impact of the boronization on the plasma performance and vacuum quality. Comparisons will be discussed to pre-boronization experiments.

As seen in figure 3.a, the integrated heat flux across all divertor target surfaces ($\int q \mathrm{d}x\mathrm{d}y$) is reduced during this density sweep from a level of larger than $\approx 3.5MW$ down to smaller than $\approx 0.7MW$. The saturation of $\int$ q is caused by the fact that a short 0.2 s time window of almost constant plasma conditions is preceding the ramp and the eventual density state is kept constant for about 0.4 s until the end of the controlled discharge. As will be discussed later in detail, this power dissipation is a result mostly due to radiative losses.

The heat flux distribution on the divertor target surfaces of one divertor module (here half-module 51) is shown in figure 3b-c for thee levels of $n_{e,l.i.}$. A homogeneous thermal unloading of the divertor surfaces is seen. Note that the maximum level of the color code in figures 3b-c is adjusted for each density level to maintain visibility of the heat flux distribution. The maximum heat flux density detected on the divertor module is reduced from $\hat{q} = 3.0MWm^{-2}$ for $n_{e,l.i.} = 9.5 \times 10^{19}m^{-2}$ at $t = 5.0s$ to $\hat{q} = 1.5MWm^{-2}$ for $n_{e,l.i.} = 10.2 \times 10^{19}m^{-2}$ at $t = 6.0s$ and finally reaches consistently values of smaller

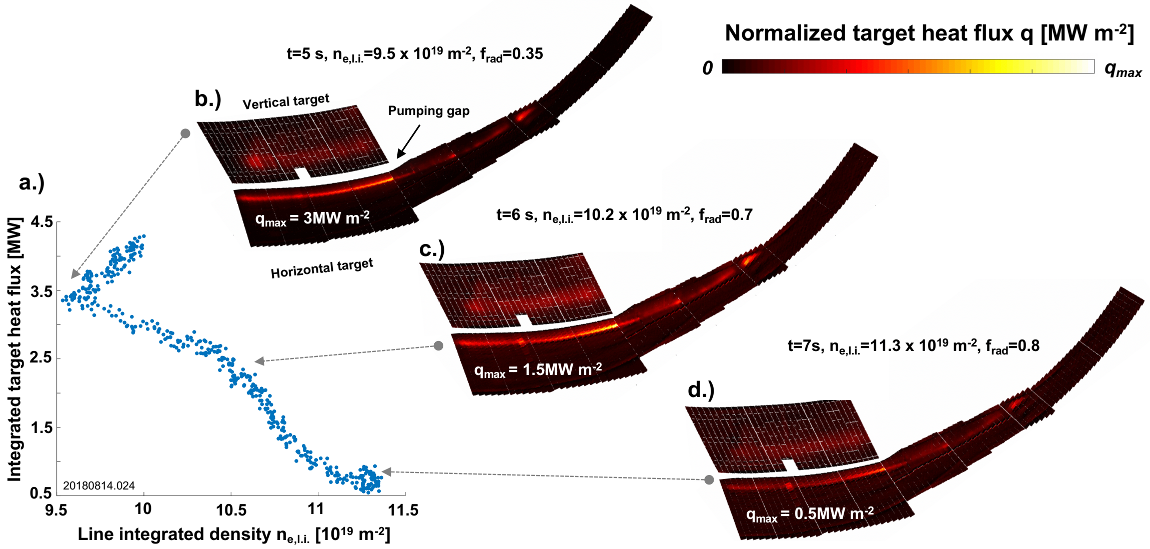

Figure 3: Experimental observation of the heat flux detachment: in figure (a) the dependence of the integrated heat flux onto all divertor target plates on the line averaged density is shown. A homogeneous thermal unloading of the divertor target plates is seen during this detachment transition by the heat flux measurements on the divertor targets in half-module 51, shown in figures part b-d.

than $\hat{q} = 0.5MWm^{-2}$ for density values above $n_{e,l.i.} = 11.3\times10^{19}m^{-2}$ at times later than $t = 7.0s$. This reduction of the maximum heat flux by almost an order of magnitude is a reliable result, which was obtained for different heating scenarios at different density levels as discussed later on. One specific metric in this transition into full thermal detachment is the fraction of power radiated by line emission of the absorbed heating power P_{ECRH} f_{rad}. This increases from $f_{rad} = 0.35$ to $f_{rad} = 0.7$ and reaches values $f_{rad} > 0.8$ for the fully thermally detached phase. It will be seen in the following that f_{rad} is a central metric because detachment access and also the divertor particle fluxes and neutral pressure levels for the island divertor correlate with it. It should be noted that the measurement of radiated powers and the spatial resolution of the radiated power distribution represents a significant diagnostic challenge [55]. The measurement uncertainty in terms of the absolute level of radiated powers is defined by the calibration accuracy as well as spectroscopic cross talk from first wall components in the bolometric measurement. Presently, an estimated measurement uncertainty of 10 % of the measured radiated power levels is used. The geometrical observation uncertainties to resolve the radiation localization will be discussed later.

The heat flux detachment was seen in experiment to correlate with f_{rad}. This correlation was also reproduced in modeling with the EMC3-EIRENE fully 3D plasma edge fluid and kinetic neutral transport code [57, 58]. This modeling was conducted

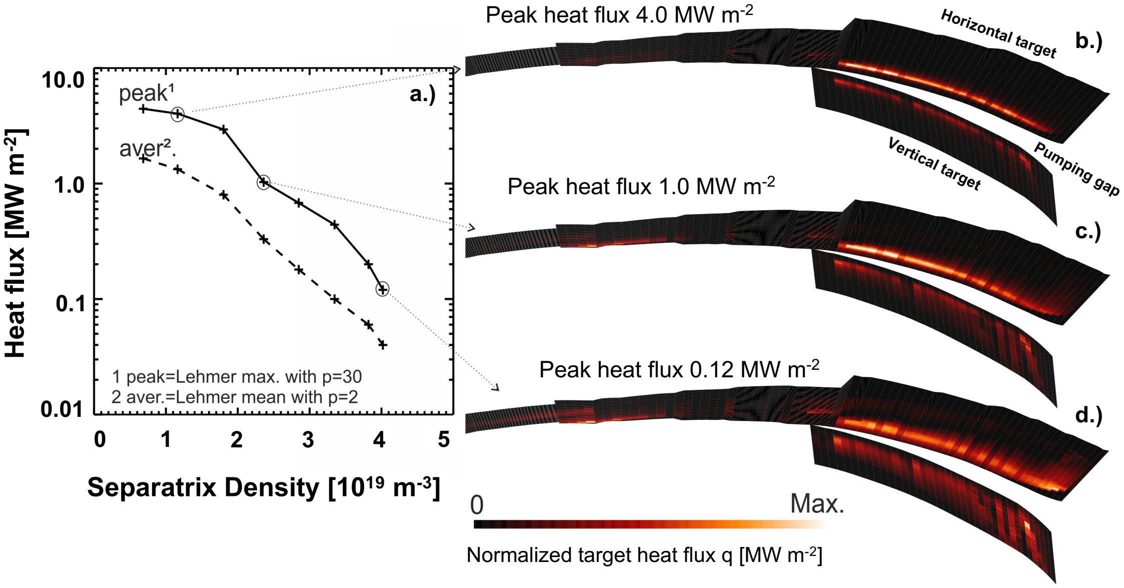

Figure 4: Heat flux detachment modeling with EMC3-EIRENE. In figure part (a), the Lehmer maximum and mean [56] for the peak and averaged heat flux is shown as a function of the separatrix density (see explanation in text). In figure parts (b-d), the 2-D heat flux distribution on the horizontal and vertical target of one divertor modules is shown for three density cases. The maximum of the color bar is adjusted for each step to show the homogeneous cooling across the entire divertor targets.

in alignment with the experimental situation to aid direct comparisons of trends in the most important parameters for detachment. More detailed matching of experimental conditions by reconstructing, for instance, radial profiles to constrain the selection of transport coefficients etc. is being addressed and will be discussed in future papers. A comparison between modeled and measured densities and temperatures at the separatrix is presented below. For the modeling utilized in this paper, an input power level of $P_{ECRH} = 5.8MW$ evenly distributed between electrons and ions was utilized and a perpendicular anomalous particle diffusivity of $D_\perp = 0.5m^2s^{-1}$ was assumed with $\chi_\perp = 3 \times D_\perp$ for the perpendicular anomalous heat diffusivity. The electron density $n_{e,s}$ at the separatrix was used as a boundary condition for the particle balance in the code. While in the numerical setup, the position of the last closed flux surface is well defined and $n_{e,s}$ can directly be determined, this parameter is very difficult to obtain in experiment with certainty. Therefore, we use $n_{e,s}$ as density value in the modeling and $n_{e,l.i.}$ as density metric in the experiment to be less susceptible to variations in the separatrix position in experiment. Details about the density $n_{e,s}$ are discussed later based on figure 14. The modeling is found to match the experiment within the error bars of the density measurement ($\approx 30\%$) and within a factor of two for T_e $(40 - 80$ eV).

In figure 4, a comparable setup of data as discussed for the experiment in figure 3, but now based on EMC3-EIRENE results with these input parameters is shown. In figure part (a), the Lehmer means [56] for the peak and averaged heat flux is shown as a function of the separatrix density. The Lehmer mean and maximum [56] is defined as $L(x) = \int x^p ds / \int x^{p-1} ds$. Here, x represents the heat flux density distribution over the entire surface s of all relevant targets. They are evaluated using with p=2 and 30, respectively. In figure parts (b-d), the 2-D heat flux distribution on the horizontal and vertical target of one divertor modules is shown for three density cases. The maximum of the color bar is adjusted for each step to show the homogeneous cooling across the entire divertor targets. The scaling of the heat flux density $q_\perp$ with $n_{e,s}$ is shown on the left and resembles qualitatively the experimentally identified reduction of more than an order of magnitude. However, the density variation in experiment was much smaller than in this first, qualitative modeling attempt, and hence the actual reduction level cannot directly be compared. An important feature of the way the thermal unloading of the divertor surfaces proceeds is jointly observed in experiment and modeling. To discuss this observation, the 2D distributions of the $q_\perp$ on the divertor targets is shown on the right, with adjusted color bar for each of the density steps. This analysis shows the same homogeneous thermal unloading of the divertor targets with increasing density, as seen in experiment, and confirms numerically the transition into full thermal detachment. This modeling setup will later be used to discuss findings on particle flux and neutral pressure build up.

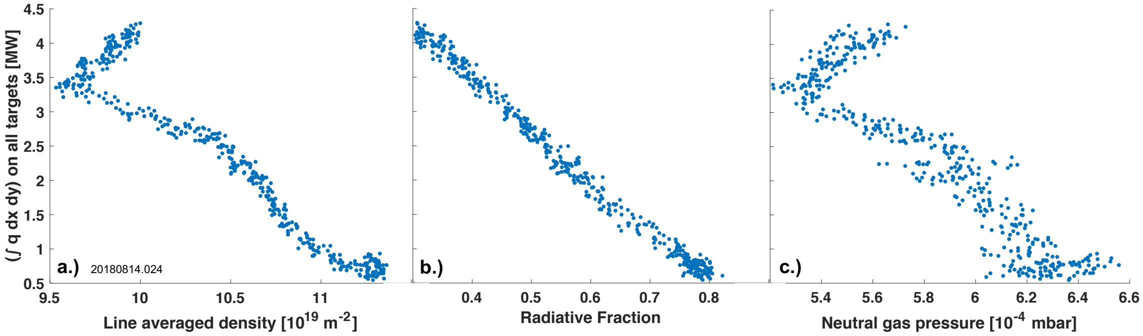

Figure 5: Integrated divertor heat flux y-axis on all plots as function of $n_{e,l.i.}$ (part (a)), the radiative fraction (part (b)) and the divertor neutral gas pressure (part (c)).

The thermal detachment itself is an important finding, but to make for a successful divertor concept more requirements of the island divertor as exhaust device have to be met. In figure 5, the integrated heat flux already discussed before is now plotted as a function of the radiated power fraction f_{rad} (figure 5.b) and of the averaged neutral gas pressure $\bar{p}_{n,div}$ across all divertor modules (figure 5.c). The averaged neutral pressure

$\bar{p}_{n,div} = (\sum_{i=1}^{3} p_{n,pump\ gap})/3$ is obtained using the three available hot cathode neutral pressure measurements located close to the divertor pump gap [59] at the end points of the island SOL discussed based on figure 2. This average is taken as representative measure for the entire set of divertor modules. This analysis exhibits two important features of this detachment regime. First, in figure 5.b, it is seen that the integrated heat flux decays linearly with f_{rad}. The start density level of $n_{e,l.i.} = 9.5 \times 10^{19} m^{-2}$ at the beginning results in a moderate level of $f_{rad} = 0.35$, which increases rapidly with increasing density to $f_{rad} > 0.8$ but well below radiative collapse of the power balance. Therefore, as will be shown later, such a moderate density swing as executed in these experiments enable reliable access to a domain in which $0.8 < f_{rad} < 0.9$ and where heat fluxes are largely vanished.

The second important observation is the $\bar{p}_{n,div}$ increases from a level of $\bar{p}_{n,div} = 5.2 \times 10^{-4}$mbar at $t = 5$s to $\bar{p}_{n,div} = 6.0 \times 10^{-4}$mbar at $t = 6$s and equilibrates at around $\bar{p}_{n,div} = 6.5 \times 10^{-4}$mbar at $t = 7$s and beyond. This $\approx 25\%$ increase in $\bar{p}_{n,div}$ is an important finding, as heat flux detachment needs to be combined with sufficient neutral pressure for stable particle and impurity exhaust. However, at this point the increase in neutral pressure with increasing density indicates increasing divertor particle fluxes during the complete thermal detachment. This would be an adverse effect with respect to maintaining divertor surface integrity, because surface erosion levels might increase with increasing overall particle flux - depending on the actual divertor plasma temperatures. Even if the divertor plasma is cooled below physical sputtering thresholds, high density immediately at the target can yield transfer of the potential energy of recombination processes and hence exceed heat flux limits [60]. Therefore, as a common paradigm, a well detached divertor shall feature detached heat fluxes and at least significantly reduced particle fluxes, to a level compatible with maintaining a sufficient neutral pressure for efficient particle exhaust [46, 61, 34]. To address this capability of the island divertor, in the following the neutral particle inventory and the divertor particle fluxes in relation to the heat flux and f_{rad} will be discussed in detail.

4. Neutral pressure build up and particle flux detachment

The build up of neutral pressure levels in the range of $2-8 \times 10^{-4}$ mbar depends on the heating power P_{ECRH} applied through a link between density and P_{ECRH}. This is shown in figure 6.a, where $\bar{p}_{n,div}(n_{e,l.i.})$ is plotted for a wide set of discharges with different heating powers, before and after the boronization, and also for two different settings of the island control coil currents I_{CC}, which control the island size and position. The set of discharges considered in the following consists also of two discharges at $P_{ECRH} = 2$ MW and $P_{ECRH} = 3$ MW from before the boronization was performed, included in figure 6.a as blue and orange traces (see labels). In these discharges, neutral pressure levels were limited to $\bar{p}_{n,div} < 10^{-4}$mbar and the plasma density was usually in the range of $n_{e,l.i.} < 5.0 \times 10^{19} m^{-2}$. After the boronization Oxygen and Carbon levels were reduced by up to a factor of 20 [26, 54], which allowed for much higher plasma density and simultaneously increased neutral pressure levels. This is visualized by the $\bar{p}_{n,div}(n_{e,l.i.})$ traces in figure 6.a from after boronization. For instance, the yellow and purple time trace represent $\bar{p}_{n,div}(n_{e,l.i.})$ at $P_{ECRH} = 2$ MW (yellow) and at $P_{ECRH} = 3$ MW (purple), i.e. at the same P_{ECRH} levels as the two previous discharges before boronization. The huge increase in the density range obtained, as well as the factor of $5 - 10$ increase in $\bar{p}_{n,div}$ from levels of $4 - 6 \times 10^{-5}$mbar before boronization, to $2 - 4 \times 10^{-4}$mbar at this power level after boronization is evident. Also, a saturation of $\bar{p}_{n,div}$ is seen once a certain density level is reached at a given P_{ECRH}. Further increasing the heating power expands the density range and yields further increased levels of $\bar{p}_{n,div}$. This is seen in the green time trace, in which $\bar{p}_{n,div}(n_{e,l.i.})$ is shown for $P_{ECRH} = 6$ MW to reach $4-5\times 10^{-4}$mbar.

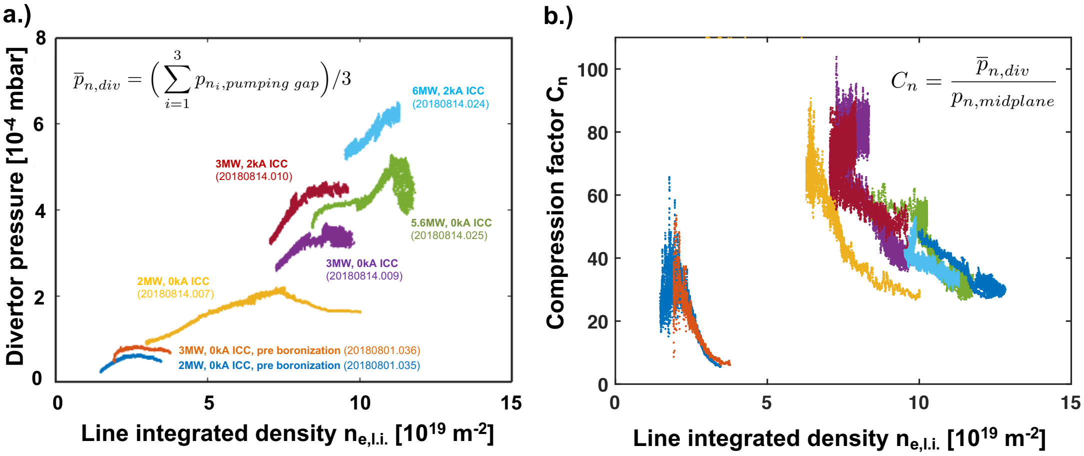

Figure 6: The neutral pressure build up with density is shown in figure part a before and after the boronization and considering three different power levels and two levels of island control coil currents I_{CC}, that is 0 kA where not otherwise indicated. In figure part b, the neutral compression ratio between the main vessel, measured with one hot cathode gauge at the outer mid-plane (i.e. the upstream position), and one in the divertor housing, i.e. the downstream position is shown.

In figure 6.b, the neutral compression ratio C_n for this sequence of discharges is shown. In a successful divertor scheme, it is important to avoid build up of high neutral pressures in the main chamber of the vacuum vessel, but neutrals need to be captured in the divertor chamber to realize stable pumping and good plasma density control. Therefore, we compare the neutral pressure in the main chamber $p_{n,midplane}$ with the averaged neutral pressure $\bar{p}_{n,div}$ obtained in the divertor pumping volume. Here, $p_{n,midplane}$ is measured by one hot-cathode gauge that is located at the upstream position of the island divertor SOL, as discussed, based on figure 2. It is located approximately 30 cm away radially from the last closed flux surface and maybe 20 cm away from the outermost flux surface of the island that forms the SOL. The result of this analysis is shown in figure 6.b as a function of the line integrated density $C_n(n_{e,l.i.})$. The color of the time traces matches the discharges discussed previously for figure part a. One can see that before boronization C_n was limited to values below 50 and reduced to below 5 for the highest densities reached in this scenario. After boronization, a much improved compression ratio of $C_n = 80 - 90$ at low density before detachment and of $C_n > 35$ during the detached regime was seen. These values show that the neutral collection in the divertor produces a downstream neutral pressures that overcomes the pressure in the main chamber by a factor of 35 and more. This is correlated with a stable density control for these plasmas and indicates a sufficient pumping capability that is established with this pressure balance in the vacuum vessel during plasma operations. The strong reduction of the compression ratio as detachment is obtained supports an increased leakage of neutrals from the divertor into the main chamber, but it is shown below that the pumping level reached is compatible with a steady state balance of fueling, pumping and stable density control for long time scales. The values of C_n are obtained with the relatively open divertor baffle structure shown in figure 1.b and c. The target structure is relatively open. The surfaces at the end of the divertor module towards the main chamber are closed by divertor closure panels [36] shown in figure 1.b. The compression ratios obtained are substantial due to the high densities in the divertor ($\approx 2.0 - 4.0 \times 10^{19}$ m^{-3}, see figure 14) at temperatures in the ≈ 50 eV range and a resulting H ionization length scale of $\lambda_{io,H} \approx 2 - 5$ mm, assuming purely atomic neutrals at thermal velocities defined by the wall temperatures. Including molecular dissociation and charge exchange can increase $\lambda_{io,H}$, but the limiting impact of low temperatures and high densities in the domain of the island during detachment is discussed later. We therefore consider $\lambda_{io,H}$ to be smaller than the island width w_{isl} at the O-point ($10 - 12$ cm) for the bulk of the neutral population. This limits the probability of a recycled neutral particle to reach the plasma core and increases the collection probability and hence efficiency of the divertor. The volume of the island that forms the divertor hence can serve as an effective means to generate such good collection efficiencies as measured here by C_n. This topic deserves more detailed deliberations and analysis, but this general finding and explanation of the effectiveness of the island divertor for good pumping was also seen in the exploration study with EMC3-EIRENE used for reference [20].

The island divertor setup at W7-X is equipped with divertor control coils. These are normally conducting, window-frame coils, which are situated inside of the vacuum vessel behind the the outer baffles that extend from the bean shaped symmetry plane into the high-iota domain of each island divertor module [6]. The island geometry can be manipulated with these coils in order to control divertor conditions. In figure 6.a, two more traces of $\bar{p}_{n,div}(n_{e,l.i.})$ are included that were obtained during applying the maximum allowable current $I_{CC} = 2$ kA to these control coils. The trace in red is the result from a discharge with $P_{ECRH} = 3$ MW and in light blue, the maximum pressure obtained is shown for a discharge with $P_{ECRH} = 6$ MW. The heat flux detachment for this discharge was already presented in the discussion of figure 3-5. This W7-X experimental program 20180814.024 will be the main analysis target in the following. It can be clearly seen that application of this level of I_{CC} yields an increase of $\bar{p}_{n,div}$ by $30-50\%$ to up to 6.5×10^{-4}mbar for the $P_{ECRH}=6$MW case (light blue line). This is a result of changing the size and shape of the magnetic island that forms the island divertor. In figure 7, a comparison is shown of the magnetic structure of the island for a case with $I_{CC}=0$ kA (figure 7.a) and $I_{CC}=2$ kA (figure 7.b).

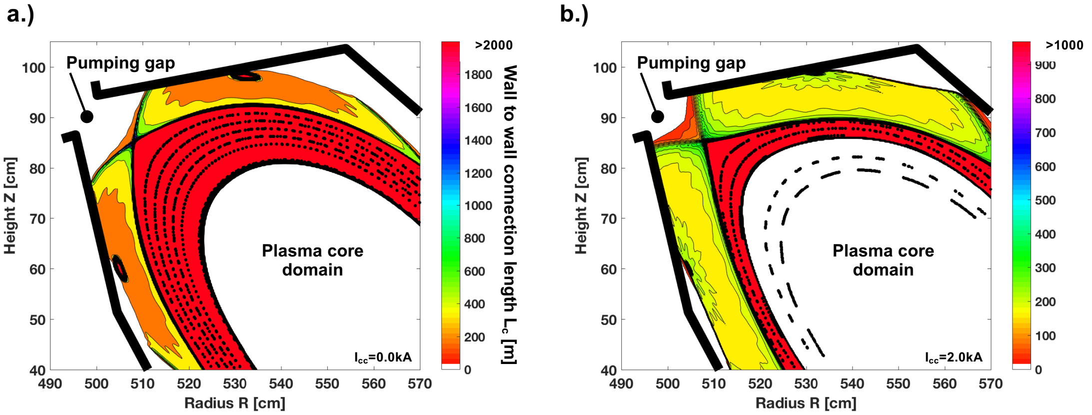

Figure 7: Structure of the magnetic island depicted at toroidal angle $\phi=12.5^o$ as wall to wall connection length L_c with (a) no control coil current $I_{CC}=0$ kA and with (b) $I_{CC}=2$ kA. The color coded L_c values were obtained from a field line tracing that was concatenated at $L_c=1000$ m. This maximal value is marked with a red color. These red field lines inside of the separatrix are therefore longer than 1000 m. At some radial point inward, the tracing was stopped. This is the white domain in the core, where flux surfaces from a Poincaré plot are included. In the outer domain, field lines in the SOL are short ($L_c<20$ m) and they are marked in white radially outward of the islands. This approach hence emphasizes the clarity of the connection length structure around the islands and all the way to the separatrix with the color code provided. Some selected L_c values are shown and referred to in the text.

These plots depict the magnetic connection length $L_c(R,Z)$ from wall to wall in this domain of the plasma obtained from vacuum magnetic field line tracing. The plasma center was not included in the field line tracing and is marked in white with $L_c=\infty$ and further out in red with $L_c>1000$ m, which was the maximum length the field line was traced for. In this domain, the field lines lay on good flux surfaces as shown in the overlaid Poincaré plot of selected surfaces as example. Passing the separatrix of the $n/m=5/5$ island, a reduction of L_c is seen with a specific substructure that reflects the fact that the magnetic islands have their own internal flux surfaces, which are intersected by the divertor targets and hence opened, yielding reducing L_c. This domain of the magnetic islands hence represents the scrape-off layer (SOL) of the island divertor. However, also a small domain with remaining good flux surfaces can be seen for the case with no control coil current in figure 7.a as the region with $L_c > 1000$ m in the island center, the so-called O-point.

Three main features can be observed when comparing these two island structures that can have an impact on where neutrals are produced, how they are distributed, and where they will get ionized. First, the location of the strike line is shifted by $\Delta s_{wall} = 5.9$ cm along the divertor target surface towards the pumping gap with an increase of the control coil current $I_{CC} = 0 \rightarrow 2$ kA. This reduces the distance between the strike line and the pumping gap entrance from $\Delta s_{gap} = 12.1$ cm for $I_{CC} = 0$ kA to $\Delta s_{gap} = 6.2$ cm for $I_{CC} = 2$ kA. This is the most intuitive reason for increased neutral pressures. A closer proximity of the main recycling domain to the neutral pump is very likely to increase neutral pressures, because neutrals born at the strike line where most of the incoming ion flux arrives are more likely to enter the divertor pumping domain through the pump gap. Second, the value of L_c in the direct vicinity of the strike line is decreased by a factor of two with this increase in I_{CC}. This can be seen when focusing on the strike line domain at the horizontal target of figures 7.a and b. For the case with $I_{CC} = 0$ kA, the yellow color on the left and cyan color on the right of the divertor leg formed by the island separatrix denote actual values of $L_c = 170$ m in the private flux region (yellow) and $L_c = 520$ m towards the island (cyan). The latter is the SOL domain and hence carries most of the heat and particle fluxes, as detected in both experiment as well as modeling. For the case with $I_{CC} = 2$ kA, theses values are reduced by more than a factor of two, i.e. red color in figure 7.b with $L_c = 60$ m in the private flux region on the left of the divertor leg and green color with $L_c = 260$ m in the SOL towards the island on the right. This could yield reduced perpendicular losses due to the shorter pathway into the divertor for the $I_{CC} = 2$ kA case, which can enhance the ratio of the amount of particles that are recycled in the divertor and build up neutral pressure to the total amount of recycled particles, denoted as collection efficiency. Last but not least, the island size grows from a distance between separatrix to target at the O-point location of $d \approx 6.5$ cm for $I_{CC} = 0$ kA to of $d \approx 10.2$ cm with $I_{CC} = 2$ kA. With typical electron temperatures T_e in the island between $10 - 40$ eV, this would provide a larger volume for ionization. Also, the outer gap between the island separatrix on the right and the vertical target, which is left open for $I_{CC} = 0$ kA is closed for $I_{CC} = 2$ kA. This might have an impact on neutral trapping in the island. Due to the closer proximity of the island divertor plasma to the vertical target, this effect on the island geometry also could result in particle fluxes on the vertical target and the upper baffle region. These fluxes are less likely to be collected in the divertor volume and hence, they do not contribute to the neutral particle compression in the divertor. These three features are consistent with the observed increase of $\bar{p}_{n,div}$ when the divertor control coils are utilized and the observed trend for increased $\bar{p}_{n,div}$ with increasing I_{CC} is in line with EMC3-EIRENE modeling as presented in [20].

To connect to this systematic exploration study, dedicated modeling with EMC3-EIRENE was conducted for the plasma scenarios considered in this paper. A density scan was investigated numerically using $P_{ECRH} = 5.8$MW with $I_{CC} = 2$kA at a particle diffusivity of $D_{\perp} = 0.5 \times m^2/s$ and $\chi_{\perp} = 3 \times D_{\perp}$. The impurity concentration is defined by a gross averaged effective erosion yield of 4% carbon flux Γ_C from the incoming hydrogen flux Γ_H. For radiative fractions $f_{rad} > 0.75$, the impurity concentration is iteratively controlled through an adjustment in this effective erosion yield to match the radiation request. This EMC3-EIRENE sequence will be used to support the initial interpretation attempts of the experimental observations of the island divertor detachment throughout this paper.

For the discharge with the highest neutral pressure levels at $P_{ECRH} = 6$MW and $I_{CC} = 2$kA (light blue curve in figure 6, W7-X program 20180814.024), a reduction of the incoming particle flux during an increasing neutral pressure is seen, for the density levels at which the heat flux is completely detached. This observation is shown in figure 8 utilizing two different measurements to infer the particle flux scaling during the density increase that yields full thermal detachment. The particle flux measurements are shown as a function of line integrated density $n_{e,l.i.}$ (figure part (a)), the radiative fraction f_{rad} (figure part (b)) and of the averaged divertor neutral pressure p_n (figure part (c)). The first measurement used is the recycling flux $\Phi_{rec,int}$ as integral flux from H_{α} measurements across the horizontal and vertical target in all ten divertor modules. The measured H_{α} line emission at $\lambda = 656.2$nm was converted into a particle flux by using an S/XB coefficient of 30 as a gross averaged value, which is constituted by a value of 15 from the atomic contribution multiplied by two due to molecules. This coefficient

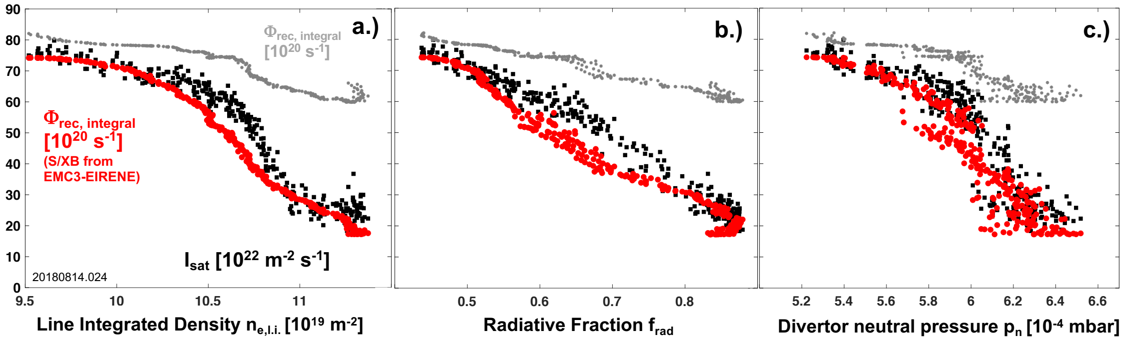

Figure 8: Particle flux measurements as a function of line integrated density $n_{e,l.i.}$ (figure part (a)), the radiated power fraction f_{rad} (figure part (b)) and the averaged divertor neutral pressure $\bar{p}_{n,div}$ (figure part (c)). The integrated recycling flux Φ_{rec} with S/XB obtained from EMC3-EIERNE modeling is shown in red and with a fixed value of $S/XB = 30$ is shown in grey. The I_{sat} trace is shown in black.

quantifies the amount of ionization source (S) per excitation (X) times the branching ratio (B), i.e. it is the conversion factor between particles and photons measured by the spectroscopic method [62]. This choice is as starting point and the value chosen is based on a similar analysis in the attached temperature range at comparable plasma edge densities in the attached regime from TEXTOR [63, 64]. As will be discussed later, the values for the electron temperature T_e in the divertor are found to be in the range of $T_e \approx 40$ eV for the attached phase and $8 < T_e < 13$ eV for the detached phase. Therefore, we consider a constant $S/XB = 30$ as a conservative assumption resulting in an upper maximum for the particle flux invoked from the H_α measurement. These maximal $\Phi_{rec,int}$ values are shown as grey line in figure 8 a-c.

Synthetic analysis of the volume integrated S/XB coefficient in the EMC3-EIRENE modeling sequence used in this paper shows during the density increase that leads into detachment an initial increase of S/XB from 23 at low density (attached conditions) to 30 at medium density (starting thermal load reduction) to 8 in the detached phase. The values of $\Phi_{rec,int}$ calculated with S/XB interpolated between these values at the appropriate density points are shown as red time trace in figure 8 a-c. The measured H_α intensity I_{H_α} on the divertor target surfaces amounts to approximately 60% of all measured I_{H_α}. The rest is seen in front of baffle structures and the carbon covered first wall panels, but not included in the integration here.

The accuracy of this use of S/XB values inferred from EMC3-EIRENE to interpret the measured H_α intensities in terms of a H particle flux is defined by the agreement in the divertor density and temperature during this density sweep. We will discuss later (see figure 14) that densities agree within 30% and T_e within a factor of two, i.e. between $40 - 80$ eV. The exact impact this temperature change brings for the S/XB coefficient depends on the detail of the atomic vs. molecular release [62, 63, 65] after the recycling process and the dominant excitation process. In the analysis of the experimental data, we have used a summative S/XB coefficient in the relevant edge temperature regime that included atomic ionization by electron impact and dissociative ionization in which a molecule is dissociated and one H atom is ionized at the same time. In EMC3-EIRENE, the EIRENE code is used to calculate the various production processes for the ions from atomic and molecular hydrogen. This information is added when we include the change of $S/XB(T_e)$ with increasing f_{rad} in the conversion of the H_α intensity into $\Phi_{rec,int}$.

To estimate the impact of the deviation in modeled and measured T_e on the S/XB, we assess the change in the ionization rate coefficient from dissociative ionization S_{DI} and atomic ionization S_{AI}, both through electron impact. Following [65] (included in Open ADAS), we find that $S_{DI}(80eV) \approx 2.5 \times 10^{-9}$ cm^3 s^{-1} $\rightarrow S_{DI}(40eV) \approx 1.5 \times 10^{-9}$ cm^3 s^{-1} and $S_{AI}(80eV) \approx 2.5 \times 10^{-8}$ cm^3 s^{-1} $\rightarrow S_{AI}(40eV) \approx 1.5 \times 10^{-8}$ cm^3 s^{-1}. This shows that the deviation in the S/XB coefficient due to the difference in T_e in modeling and experiment lay within a factor of two and this will also include any deviation from the density uncertainty. This would affect the absolute value of the recycled particle flux $\Phi_{rec,int}$ inferred through the S/XB method. However, as we are looking mostly for the trends of one parameter (here $\Phi_{rec,int}$) with respect to a control parameter (here f_{rad} or $n_{e,l.i.}$), it should be noted that S_{DI} and S_{AI} that are used for reference decrease at comparable rates when going from $T_e = 40 - 80$ eV down to $T_e \approx 10$ eV. Therefore, we consider the uncertainty in the absolute value of S/XB and its scaling with T_e in this temperature range as small. Accordingly, the synthetically inferred function of $S/XB(T_e)$ used in the reconstruction of the recycling flux provides us with a quite robust trend for $\Phi_{rec,int}$, that will be shown soon to also be compatible with the ion saturation current on the divertor target. Below 10 eV, the S/XB undergoes significant changes that are different for different ionization chains and a more sophisticated analysis is required to scale S/XB in such an analysis. A detailed analysis of the recycling fluxes with mapping of temperature data onto the spatial domain of dominant H_α emission is necessary to quantify the particle source and its distribution in detail.

The second method utilized to quantify the evolution of the divertor particle flux with increasing density is the ion saturation current I_{sat} measurement from a Langmuir probe close to the strike line. The nearest Langmuir probe is for the SDC with $I_{CC} = 2$kA is 5 cm away from the strike line and hence does not provide a direct flux measurement at the strike line. The I_{sat} values are shown as black traces in figure 8 a-c. A clear decrease of both particle flux measures with increasing $n_{e,l.i.}$ is seen in figure 8.a. For I_{sat}, a reduction from 75×10^{22} m^{-2} s^{-1} can be seen with at first a gradual decrease that above 10.5×10^{19} m^{-2} yields a very rapid decay during the further increase in density to eventually 25×10^{22} m^{-2} s^{-1}. This curve shape is resembled by the $\Phi_{rec,int}(t)$ time trace that was folded with the EMC3-EIRENE prediction of the S/XB conversion factors from 75×10^{20} s^{-1} to 18×10^{20} s^{-1}.

This decrease of the particle flux measurements to 30% of the attached values is a clear sign for detachment of the particle fluxes. Considering the evolution of these particle flux measurements with f_{rad}, as shown in figure 8.b, a linear decrease is seen when f_{rad} is increased from 0.4 in attached conditions to 0.85 in the final detached state. This needs to be compared to the linear decrease of $\hat{q}_\perp(f_{rad})$ as discussed before. The reduction in particle flux reduces the convective heat flux that contributes with less than 20% to the divertor heat flux. The reduction in T_e discussed before and in more detail based on figure 14 below, shows the dissipative contribution to the heat flux reduction. The continuous cooling of the island divertor domain due to radiation hence is a main driver of the reduction in the heat flux. The significant reduction of the measured particle flux comes alongside with an increase of the averaged divertor neutral pressure $\bar{p}_{n,div}$ by 20%, as seen in figure 8.c. This beneficial combination of particle flux reduction combined with maintaining and even increasing a substantial level of neutral pressure is promising in view of maintaining good pumping while reducing heat and particle loads to the divertor.

The result of the EMC3-EIRENE modeling sequence for the dependence of the particle recycling flux on f_{rad} is shown in figure 9 in direct comparison to the experimental measurements. In figure 9.a, modeling results of the recycling flux (red curve with axis on

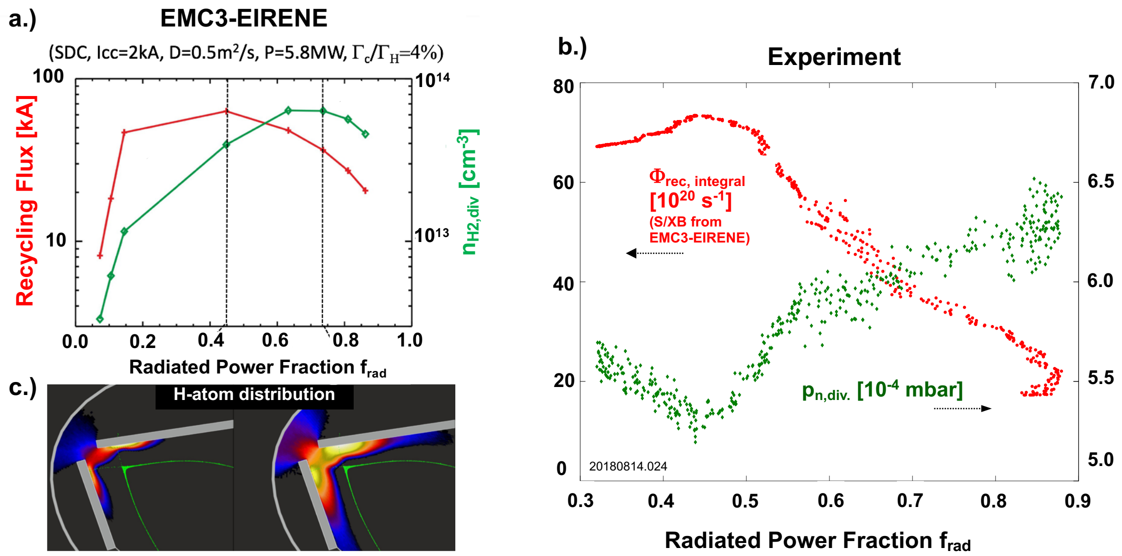

Figure 9: Particle flux link to the recycling flux from modeling (part a), the H-atomic distribution (part c, $f_{rad} = 0.45$ (left) and $f_{rad} = 0.75$ (tight)) and the direct comparison to the experiment (part b). In figure part c, the most intense atomic neutral density is shown in yellow, with red being intermediate values and blue being low values.

the left) and the molecular hydrogen density in the divertor $n_{H2,div}$ (green curve with axis on the right) are shown as a function of f_{rad}. It is seen that while the recycling flux first increases for low $f_{rad} < 0.2$, then saturates for intermediate $0.2 < f_{rad} < 0.5$ and starts to roll over and decrease for $f_{rad} > 0.5$, the neutral density in the divertor measured by $n_{H2,div}$ keeps increasing even beyond $f_{rad} > 0.5$ and only starts to decline for radiation fractions of $f_{rad} > 0.8$. A very similar behavior is also seen in the experiment.

In figure 9.b, a comparable makeup of representative measurements for these quantities from modeling is shown. In green with axis on the right, the averaged neutral pressure in the available divertor modules $\bar{p}_{n,div}$ discussed before is shown for the reference experimental program with the highest neutral pressure values and full thermal detachment (light blue curve in figure 6.a, W7-X program 20180814.024). The integrated recycling flux $\Phi_{rec,int.}$, obtained by including the volume integrated S/XB scaling into detachment from EMC3-EIRENE is shown as red curve with same axis on the left. All quantities are plotted as a function of the radiated power fraction f_{rad}. This display of the experimental measurements resembles the numerical finding. The low radiative domain is not accessible at this heating power in the experiment, as will be discussed later, and the experimental scenario starts with saturated particle fluxes for $0.3 < f_{rad} < 0.4$ at a of neutral pressure of about 5.5×10^{-4}mbar. For $f_{rad} > 0.4$, the corrected $\Phi_{rec,int.}$ decays rapidly, as also discussed based on figure 8. At the same time, the divertor neutral pressure starts to increase to a level of 6.3×10^{-4}mbar at a level of $f_{rad} = 0.8$. We will show later that this discharge scenario was stable in this regime and was maintained for up to 28s.

The origin of this increase in neutral pressure with declining divertor target particle fluxes can be understood with an intuitive model for the ionization distribution inside of the divertor. Increasing f_{rad} in the divertor yields decreasing temperature which increases the mean free path of neutral particles to ionization $\lambda_{io} = v_n/(n_e < \sigma v > (T_e))$. As the strike line resides at some distance from the pump gap, there is an optimum position of the strike line location with respect to the pump gap, to facilitate neutrals entering the pump domain instead of approaching plasma edge regions where they get ionized again. In figure 9.c, the neutral hydrogen atom distribution in the vicinity of the pumping gap is shown from EMC3-EIRENE modeling for $f_{rad} = 0.45$ and $f_{rad} = 0.75$. It can be seen that the distribution of neutrals widens as f_{rad} increases, which provides on average more neutrals to the pumping gap than before. This behavior can be parametrized by a simple intuitive model (see also discussions in [20]) where the neutral particle flux into the divertor pumping gap $\Gamma_i^{H_0} n$ is an exponential function $\Gamma_{in}^{H_0} \propto \Gamma_{ef}^{H^+} \cdot exp(-F_a)$ of the ion efflux from the plasma $\Gamma_{ef}^{H^+}$ that is defined by a decay parameter $F_a = \bar{l}_{gap}/\bar{\lambda}_{io}$ based on the ratio of the averaged distances to the gap $\bar{l}_{gap}$ and the averaged $\bar{\lambda}_{io}$. While $\bar{l}_{gap}$ is defined by the magnetic configuration, including the divertor control current I_{CC}, $\bar{\lambda}_{io}(Te)$ is through the temperature dependence of the rate coefficient directly linked to f_{rad}.

This comparison of experimental and numerical findings hence provides substantial evidence that the radiated power fraction in W7-X dissipates power such that thermal detachment can be reached and at the same time regulates the divertor conditions such that access of neutrals to the pumping domain is facilitated even under conditions of diminished target particle fluxes due to reduced local ionization. This has two aspects. One is the level of neutral particle leakage from the baffle domain into the main chamber. Do to imperfections in the baffle closure, neutrals that are collected can stream back into the main chamber and contribute to the main chamber pressure and hence the upstream particle source. The actual effective neutral particle leakage is matter of ongoing gas balance analysis, but from geometrical considerations of an estimate of the gaps between baffle panels to the opening area of the pumping gap, it is thought to range between $5 - 30\%$ of the collected neutrals, depending on the actual neutral pressure [36]. Second, neutrals that recycle and are not collected in the neutral pumping domain are represented back to the plasma where they can be ionized and contribute to the plasma ion source. The questions remains, which mechanism keeps this ionization particle source domain bound to the island divertor region and prevents the ion particle source to expand upward towards the plasma core domain? This is experimentally very challenging to resolve as it requires a high resolution measurement of the separatrix density. In [20], arguments are provided based on EMC3-EIRENE modeling that high density and low temperature across the width of most of the island facilitates charge exchange in this domain. The mean free path until a charge exchange event occurs in this domain can be described as $\lambda_{CX} = v_{i,th}/(n_i < \sigma\nu >_{CX})$. If $\lambda_{CX} < w_{isl}$, the neutral transport is defined by a diffusive process through charge exchange collisions. The diffusion coefficient for this transport process would be the product of $\lambda_{CX} \cdot v_i \propto T_i/n_i$. The diffusion of recycled neutrals towards the core domain would hence be reduced for high density and low temperatures in detached conditions. This process is able to trap the recycled neutrals in the divertor domain and increase the probability to be collected and build up neutral pressure. This intuitive thinking is confirmed by repeating an EMC3-EIRENE simulation with the CX-reaction switched off. The absence of the CX process, and thus the disappearance of the associated diffusion process, facilitates neutral penetration across the islands and leads to a significant reduction in neutral density near the targets. Detailed further modeling of this aspect is commencing and will be published in future papers.

5. Characteristics of plasma radiation and the link to divertor conditions during the detachment transition

Already in figure 6, it could be seen that the accessible density range depended on the heating power P_{ECRH}. In figure 10.a, the radiated power fraction f_{rad} is plotted as a function of the line integrated density $n_{e,l.i.}$ for the experimental scenarios considered before. In orange, $f_{rad}(n_{e,l.i.})$ is plotted for the $P_{ECRH} = 3$MW case before the boronization. With a density increase from $2 \times 10^{19}\text{m}^{-2}$ to $4 \times 10^{19}\text{m}^{-2}$, an increase in f_{rad} from

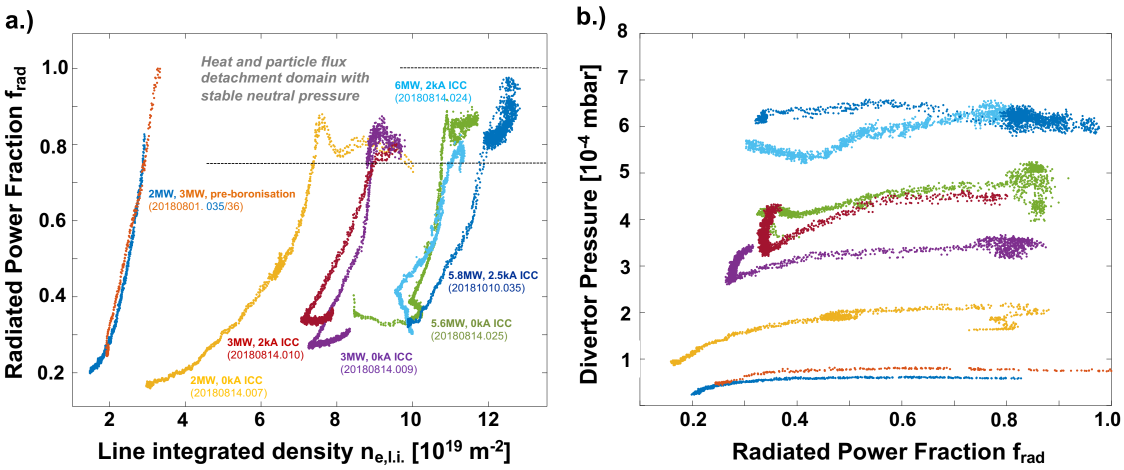

Figure 10: Radiative fraction and link to the line integrated density (part (a)) and neutral pressuref_{rad} (part (b)). Please refer to figure 6 for the discharge numbers.

0.25 to 1.0 is seen. These discharges featured thermal detachment as well as all power was dissipated by radiation, but no substantial neutral pressures were accessible [26].

As discussed before, the density range which was reached increased by a factor of $4-5$ after boronization. This is seen by the black, green, and light blue curves of $f_{rad}(n_{e,l.i.})$, which were operated with $P_{ECRH} = 3, 5.8$ and 6.2 MW respectively, and the later experimental program was operated with $I_{CC} = 2$kA (reference program W7-X 20180814.024). It can be seen that the density range accessed was defined by P_{ECRH} and that a small density increase for each case was sufficient to increase $f_{rad} > 0.8$. In this range, full thermal detachment was seen combined with substantial neutral pressures, which are defined by the density.

This is shown in figure 10.b, where the averaged divertor neutral pressure $\bar{p}_{n,div}$ is depicted as a function of the radiative fraction f_{rad} for the discharges after boronization. This set includes another discharge at $P_{ECRH} = 5.8$MW and $I_{CC} = 2.5$kA. One can clearly see increasing $\bar{p}_{n,div}$ with P_{ECRH}, and the discussion before showed that the reason is the link between $n_{e,l.i.}$ and P_{ECRH}. The actual reason for this link is under investigation, but initial results from gas balance measurements show that these discharges are operated with a saturated wall that desorbs particles at the beginning and hence the density level is set by the initial release of particles during the start of the discharge. Because the experiment was aimed on accessing high density conditions, these density levels were utilized to push into the higher radiation domain to access detachment. Further analysis of the gas balance and particle balance to understand the fueling conditions for the density dependence on P_{ECRH} are ongoing.

5.1. Carbon radiation levels and location during the detachment transition

The line emission establishing the strongly increasing power dissipation with density is born from the intrinsic impurity carbon. An extended investigation on how to use seeded impurities for power dissipation control in the island divertor is presented in [66] and [67]. In figure 11, the line emission from double ionized C (CIII, figure 11.a), tripple ionized C (CIV, figure 11.b) and five fold ionized C (CVI, figure 11.c) is shown for the experimental reference scenarios before and after boronization and for the $P_{ECRH} = 3$ MW with $I_{CC} = 0$kA and 6MW with $I_{CC} = 2$kA. This measurement is taken with the High Efficiency eXtreme ultraviolet Overview Spectrometer (HEXOS) spectrometer [68]. The line of sights of the four separate spectrometers that form the HEXOS system intersect the plasma under different angles, from nearly normal to grazing incidence to the plasma cross-section. The radial location of the emission measured is defined by its charge state and hence by the plasma density and temperature profiles as well as the impurity species distribution.

All three carbon charge states exhibit a nearly cubed dependence on $n_{e,l.i.}$. This means, the higher power scenario connects closely to the lower power scenario for the emissivity of all three charge states. Only the light blue curves for the only discharge scenario with $I_{CC} = 2$kA at $P_{ECRH} = 6.2$MW (W7-X experimental program 20180814.024) features some slight offset. This characteristic overall dependence of the carbon emission I_{C-i} for the charge states $i = III, IV, VI$ is consistent with the observation of a seamless density scaling of the divertor neutral pressure as well as the heat flux reduction discussed at the beginning. During the detachment transition, the lowest line emission I_{CII} of the lowest carbon charge state moves inward to be located just outside of the last closed flux surface (LCFS). This is shown in figure 12, in which I_{CII} obtained from line emission at $\lambda = 712.2$nm is plotted as a function of the distance d from the divertor target (x-axis) and the time t (y-axis). This measurement was taken in a discharge with very similar setup parameters as the reference discharge at highest pressure.The visible spectrometer setup used for this measurement views parallel to the horizontal divertor plate and is also used for the spectroscopy for the He-beam line ratio spectroscopy [69]. The input power was $P_{ECRH} = 5.8$MW and the island control coil current was $I_{CC} = 2$kA as well. The density increase to reach detachment was controlled by density feedback to cross the detachment transition rapidly at $t = 2.1$ s, as marked in figure 12.

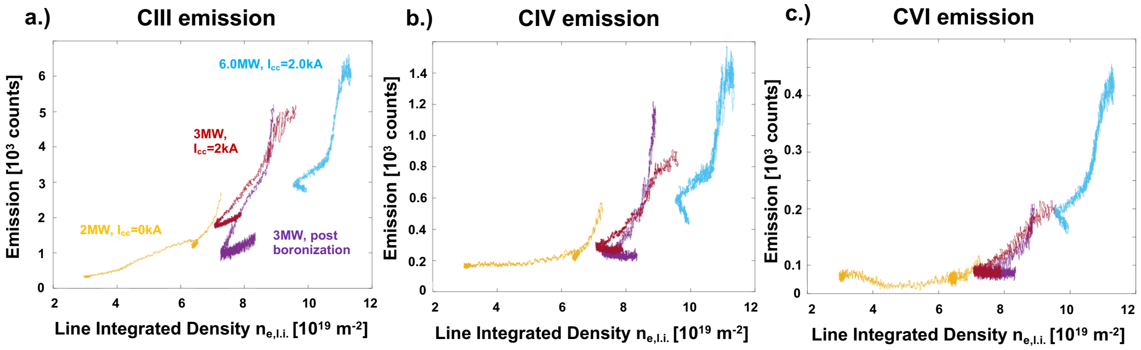

Figure 11: Carbon line emission for CIII, CIV and CVI during increase of the line integrated density $n_{e,l.i.}$ for the experimental reference cases discussed before. Please refer to figure 6 for the discharge numbers.

Before this point in time, the maximum of I_{CII} was located closely to the target plate and featured a very rapid decay away from the target plate. After the detachment transition, this maximum of I_{CII} is located at $d = 8$cm, which is just outside of the LCFS, i.e. from the side of the divertor target still just inside of the island. This indicates strong cooling of the island divertor domain and supports the idea of reduced temperatures which increase λ_{io} and hence facilitate the collection of neutrals as well as shifting the ionization distribution in the island which results in diminished particle fluxes. Also, it can yield adjustment of local temperatures and densities at the separatrix such that charge exchange at this region between the divertor and confined plasma

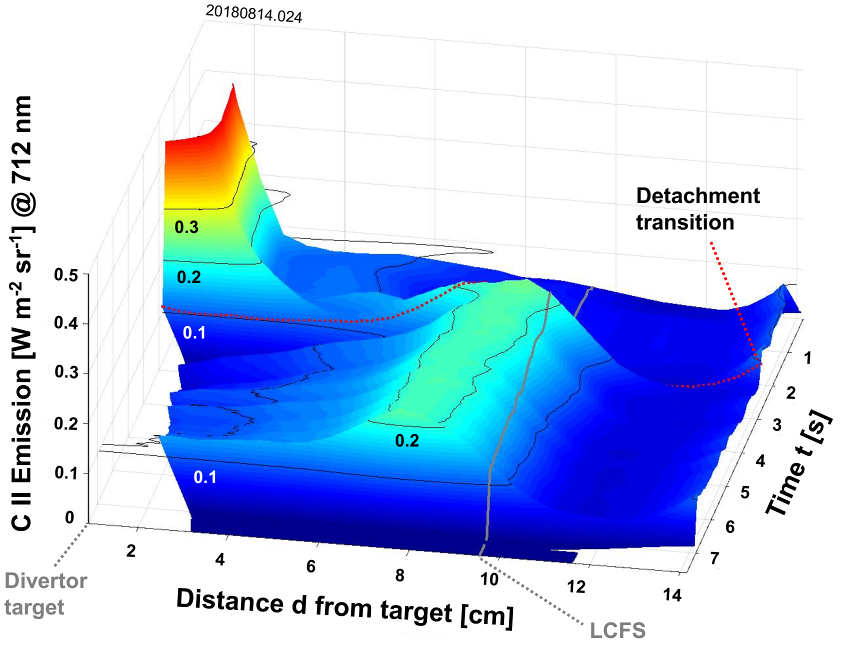

Figure 12: Carbon radiation front measured as $I_{CII}(d,t)$ as function of the distance d from the target and time t during the transition into detachment at $t = 2$s.

domain is enhanced as suggested in [20]. However, as discussed before, this is circumstantial evidence and will need a dedicated modeling effort and improved diagnostic capabilities at the separatrix for future experiments.

The electron temperature distribution in front of the divertor is measured by the thermal helium beam diagnostic in the divertor [70, 71] as shown in figure 13. Here, the electron temperature $T_e(d,t)$ in front of the divertor target is plotted as function of the distance d from the target and time t. Iso-thermal layers are included in this graph for better visualization of the shift of the temperature front during detachment. It can be seen that the $T_e = 15$eV layer is shifted from a position about $d = 4$cm away from the target before the detachment transition at $t = 2$s inward by about $6-7$cm at detachment and nearly reaches the LCFS, which is included as grey line. This measured inward shift of T_e after the transition into detachment is in agreement with the observed shifts in the CII radiation layer as well as with the reasoning for the increased neutral pressure collection in the highly radiative and eventually detached cases discussed before.

To investigate plasma electron density n_e and electron temperature T_e in the island divertor more quantitatively, the evolution of both with the radiative fraction f_{rad} is plotted in figure 14 as $n_e(f_{rad})$ (figure 14.a) and $T_e(f_{rad})$ (figure 14.b) at the position of the island O-point (green trace, diamond markers) and ≈ 2 cm radially outside of the separatrix (red, circle markers) measured with the divertor Helium Beam system [69].

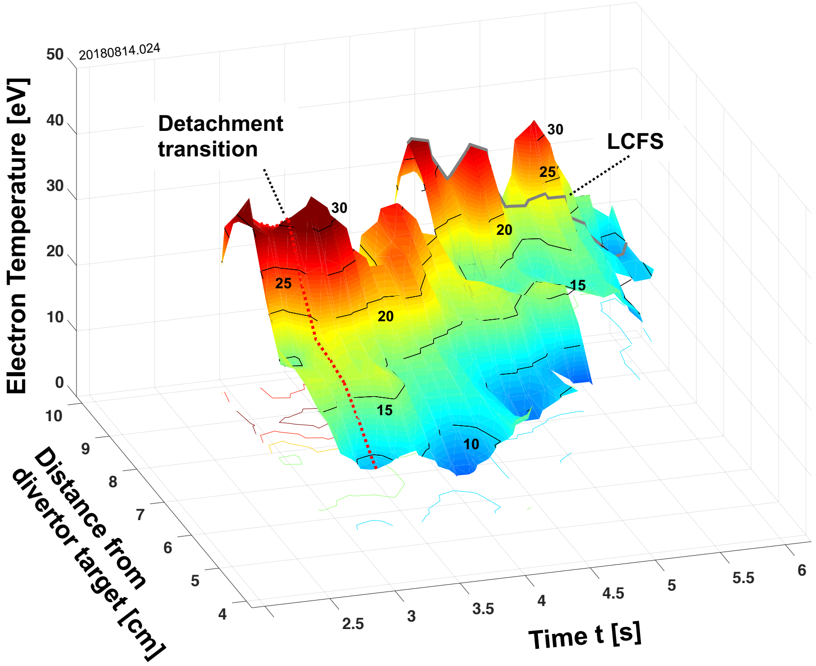

Figure 13: Electron temperature $T_e(d,t)$ in between the divertor target and the separatrix as function of the distance d from the target and time t after the transition into detachment. The radiated fraction f_{rad} increase from 0.3 to 0.8 in between $t = 2.5 - 6.0$. The areas with missing data points are due to ionization of the helium diagnostic gas injection preventing sufficient line intensity for the line ratio technique utilized [72].

The according measurements from the Thomson scattering system [73, 74] are shown as black, open circles as well in both figures. These measurements are extracted from the observation of the scattered laser system in a channel that integrates across ≈ 3 cm radially just outside of the separatrix. The density measurements of both diagnostic systems agree within the measurement uncertainties. The T_e measurements from the Thomson scattering system are a factor of $1.5 - 2.5$ above the values measured with the Helium Beam system. This deviation between both systems was also discussed in systematic comparison of these measurements [75] and on other devices (see e.g. [72]) and are matter of ongoing work to improve the Collisional Radiative model used to convert measured He emissions into n_e and T_e. These measurements provide us with a separatrix T_e range of $40 - 100$ eV at $f_{rad} = 0.35$ that is reduced to a T_e range of $20 - 40$ eV at $f_{rad} = 0.7$, after which no reliable data can be obtained with the Helium Beam system anymore. This continuous decrease of $T_e(f_{rad})$ is also seen at the O-point domain (green markers). $T_e(f_{rad})$ is measured to reduce with $\approx$ 5eV/0.1 in f_{rad} going from 40/30eV at $f_{rad} = 0.3$ to 20/18eV at $f_{rad} = 0.7/0.5$ for the separatrix and O-point region, respectively. The decay $T_e(f_{rad})$ for the Thomson scattering measurement is a factor of two faster, going from an averaged value $\hat{T}_e \approx 90$ eV at $f_{rad} = 0.3 - 0.35$ to $\hat{T}_e \approx 40$

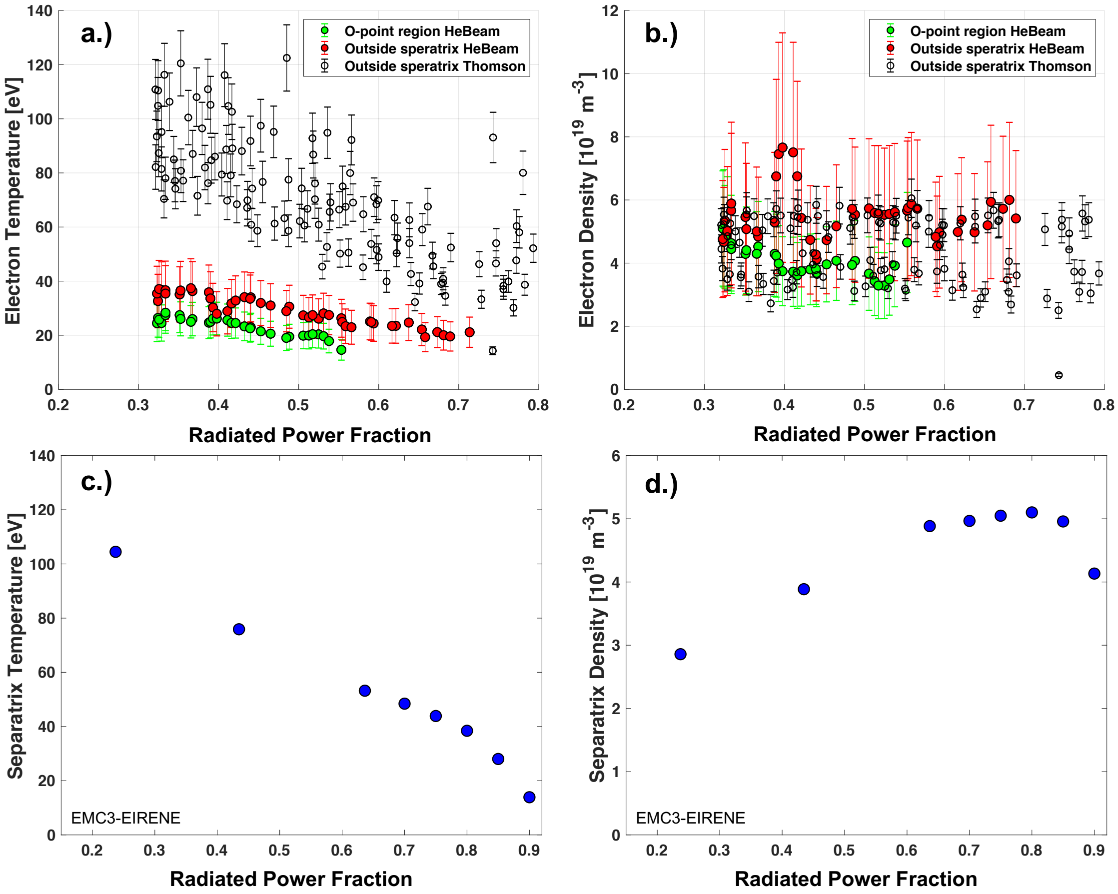

Figure 14: Electron density $n_e(f_{rad})$ and temperature $T_e(f_{rad})$ from experiment (figure part a and b) and from EMC3-EIRENE modeling (figure part c and d). For the experiment, $n_e(f_{rad})$ and $T_e(f_{rad})$ are shown at the O-point of the island (green markers) and at the separatrix (red markers). For the modeling, we show $n_e(f_{rad})$ and $T_e(f_{rad})$ at the separatrix for reference.

eV at $f_{rad} = 0.75 - 0.8$ at a rate of $\approx 10\text{eV}/0.1$ in f_{rad}. The meaning of this reduction rate of T_e for the trend-based discussions of the detachment access in this paper will be discussed later. The density is approximately constant in the experiments at 4.0×10^{19} m^{-3} for the O-point and 6.0×10^{19} m^{-3} for the LCFS. More details about this diagnostic and the SOL profile properties with the island divertor at W7-X can be found in [69, 75].

For comparison, the EMC3-EIRENE results at the separatrix are also shown for $n_e(f_{rad})$ (figure 14.c) and $T_e(f_{rad})$ (figure 14.d). These numerical results are compared to the according measurements that were discussed before. They are also relevant for the interpretation of the H_α radiation to infer a divertor particle flux through the S/XB formalism and also for the initial explanation of the substantial neutral pressure that has been maintained even while reducing the particle flux on the target. The continuous reduction of $T_e(f_{rad})$ seen in the measurement is reproduced in EMC3-EIRENE going from $T_e = 80$ eV at $f_{rad} = 0.4$ to $T_e = 40$ eV at $f_{rad} = 0.8$. This shows a continuous cooling of the plasma around the last closed flux surface while progressing to higher power dissipation levels. A cooling rate of ≈ 10 eV/0.1 increase in f_{rad} is seen that compares well to the Thomson scattering measurement results discussed before. For higher radiation levels, a very rapid further drop occurs that resembles the sudden expansion of the radiation front into the core plasma as discussed in [20] and that is also the driver for the thermal detachment without high neutral pressure reported in [76]. The separatrix density $n_e(f_{rad})$ in the modeling increases quite rapidly up for $f_{rad} = 0.4-0.5$ and then levels off to an almost constant level of 5.0×10^{19} m^{-3}. This also is comparable to the almost constant density in the measurement for this range in f_{rad}. The radiation distribution that causes this cooling effect is discussed in the next section.

The quantitative comparison of the T_e and n_e values shows that the measured temperatures from the Helium Beam are about a factor of two smaller than the modeled values and the measured density is approximately 20% higher than the saturated density level in the modeling. T_e measurements from the Thomson Scattering system agree within the measurement uncertainties with the modeled parameters. These are initial results from a direct comparative EMC3-EIRENE study that is going on. As described before, the input was adapted to general control parameters of the discharge such as the $n_{e,l.a.}$ value and P_{ECRH}. Canonical guesses for the transport coefficients for particle $D_\perp = 0.5$ m^2 s^{-1} and heat diffusion $\chi_\perp = 3 \times D_\perp$ were used. The C impurity abundance was defined by an overall sputtering yield of 4% of the incoming particle fluxes and adjusted for $f_{rad} > 0.8$ to reach the high radiation levels, i.e. the relative C source was increased beyond the level of a 4% yield. The comparability with experiment of T_e within less a factor of two - depending on the measurements considered - and of n_e within 20% is hence considered a satisfying agreement for the purpose of this paper.

The main result from this comparison is the observation of continuously reduced divertor plasma temperatures from the target to the separatrix domain. It shall be noted that the T_e values shown in figure 14 show $T_e > 10eV$ for the detached state for the plasma domain from the O-point radially inward to the LCFS. This measurement location is within 10 cm distance to the target plate. This suggests a detachment at rather high T_e values that does not require volume recombination as additional energy and momentum loss channel. Initial spectroscopic survey of H lines to detect recombining features in the plasma in front of the targets did accordingly not provide evidence for volume recombination. Based on this, the linear relationship between T_e in the SOL and f_{rad} is consistent with increasing radiation due to increasing $n_{e,l.i.}$ at the upstream position. The detachment discussed in this paper hence seems to be governed by the radiative losses and not by additional energy losses usually present in cold, dense tokamak divertor detachment regimes [38]. The stability of the core plasma parameters during this dissipation process will be discussed in the next section.

Measuring the exact spatial distribution of the radiated power is very difficult due to the 3D nature of the plasma edge layer and limited access to the plasma through the cryostat. However, a bolometer system is available at W7-X to measure the radiation distribution [71, 55] and this measurement enables to assess the location of the dominant radiation domain. In figure 15, the averaged line emissivity measured with a bolometer, which is located in a triangular poloidal cross-section and has horizontal lines of sight, that is free of divertor components. Because the divertor target plates are the dominant source of radiating impurities after boronization, it is important to understand the location of the bolometer to the divertor modules. The toroidal distance in the SD-configuration to the neighboring bean shaped planes in which the next divertor module starts is $\pm 36^o$ equaling ≈ 40 cm and the distance to the nearest divertor high-iota part in which each divertor module ends is $\pm 8^o$, equaling ≈ 10 cm.

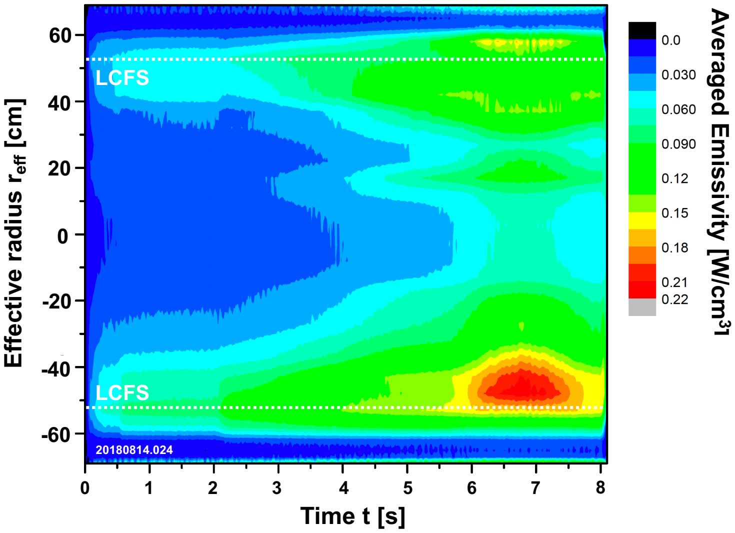

Figure 15: Radiation distribution at one poloidal plane measured with the horizontal bolometer system at W7-X [55]. The position of the Last Closed Flux Surface (LCFS) is marked as white dashed lines for orientation.

We consider again the main analysis target discussed in this paper (W7-X program 20180814.024). This discharge transitions with a long density ramp into the regime with $f_{rad} > 0.8$ and detachment at around $t = 6.5$s. The radiation distribution measured with a horizontal bolometer [55] shown in figure 15 as a function of time, indicates a gradual increase of the radiation and a growth of the radial extend of the radiation zone. However, the closest magnetic connection to the divertor module occurs in the upper region at $r_{eff} = 52$cm, where for $t > 6$s a majority of the radiation intensity is located. This agrees with the observation of strong CII emission at the island separatrix and is in support of a significant trapping of the C radiation at the transition between island and the confined plasma domain. The approximate position of the LCFS marked as a white dashed line in figure 15 is for the standard divertor configuration with $I_{CC} = 0$ kA. However, the experimental program considered here was operated with $I_{CC} = 2$ kA, which results in an inward shift of the separatrix location by about 5 cm, as discussed previously based on figures 7 a and b. A localization of the dominant fraction of the radiative losses at the island separatrix, i.e. in some narrow layer around the LCFS was also seen for discharges before boronization, where high level of power dissipation due to Oxygen enabled access to thermally detached plasma regimes at low density [76]. Also, in LHD it was seen that a magnetic island located in the stochastic layer around the confined domain is capable of trapping the impurities well enough to aid localization of the power dissipation and stabilize detachment [77, 78]. The localization of the narrow layer in which a significant amount of the radiation occurs just around the separatrix implies a challenge for the resolution of the amount of radiated power from inside and outside of the confine plasma domain. Exactly determining the amount of radiation emitted from inside and from outside of the LCFS is important in the future. This measurement is presently not possible due to limited spatial resolution of the bolometer systems. Using the LCFS position as indicated now to calculate the radiation in the SOL during detachment results in $P_{rad,SOL} = 35\%$. It is also noticeable that while $P_{rad,SOL}(t)$ stays constant during the detachment, $P_{rad,core}$ increases in between $5.7 - 7.8$ s to decay before the end of the discharge. This can be seen by the increase of the radiated power in this time window as the lower separatrix in figure 15.

The distribution of the total radiated power $P_{rad}(R, Z)$ around the islands can presently only be addressed numerically due to the limitation in diagnostic capabilities discussed before. We again use the EMC3-EIRENE modeling sequence as discussed before to investigate the general trends. It was pointed out already that there are uncertainties in matching the experimental data in detail, but it was shown that the modeling and experiment agrees within at least a factor of two in T_e and within 30% for plasma density. This is a sufficient agreement to investigate the dependence of $P_{rad}(R, Z)$ on f_{rad}, because the uncertainties in the ionization length $\lambda_{C,io}$ for Carbon between $40 - 80$ eV are small. Considering for simplicity of the argument electron impact ionization on C as discussed in [79], it is seen that the cross section $\sigma_{e,C,io}$ increases from $\sigma_{e,C,io} \approx 2.15 \times 10^{-10}$ m^2 at $T_e = 40$ eV to $\sigma_{e,C,io} \approx 2.25 \times 10^{-10}$ m^2 at $T_e = 80$ eV. This is a change of less than 10%. This is well within the uncertainty of the other parameters that determine the ionization length $\lambda_{io} = v_{th}/n_e < \sigma_{e,C,io} v >$, i.e. the C impurity thermal velocities and n_e. Therefore, we consider the modeled $P_{rad}(R, Z)$ in the vicinity of the island as representative for the scenario analyzed. This applies under the purview of a comparison between experimental and numerical trends when plasma density and f_{rad} are increased and the detached state is reached. Further refinements of this experiment to model comparison to obtain a quantitative match will be presented in future papers. This effort relies mostly on improvements of diagnostic capabilities that are being prepared for the next operational campaign of W7-X.

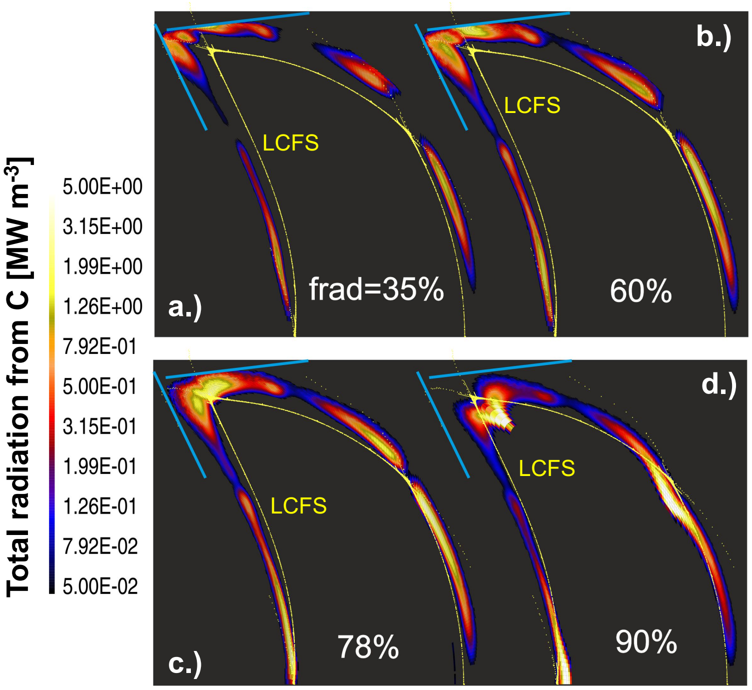

Figure 16: Radiation distribution at the poloidal plane in the bean shaped cross-section modeled with EMC3-EIRENE for four different levels of radiated power, starting from 35% in figure part (a), increasing to 60% in figure part (b) to 78% in part (c) and ending at the high radiation case of $f_{rad} = 0.9$ in figure part d.

In figure 16, the evolution of $P_{rad}(R, Z)$ of carbon during an increase of f_{rad} from 35% to 90% is shown. The same modeling parameters as introduced earlier were used. In general, for $f_{rad} < 50\%$, intensive radiation mainly originates in the outer radial region where the plasma interacts with the divertor plates. With increasing f_{rad} from 50% to 80%, the zones of intensive radiation move radially inwards and approach the X-points of the magnetic islands poloidally. Up to this point in f_{rad}, the radiation is well located in the edge islands, radially outside the last closed flux surface. This is the radiation level for which stable detachment with high neutral pressures were found in the experiment. When rising f_{rad} above 80%, the separated radiation areas finally arrive and merge together at the X-points establishing a poloidal radiation belt with clear radiation peaks around the X-points and hence the radiation fronts start to penetrate into the confinement region. This radiation level agrees with the observation of a noticeable reduction of the stored energy in the experiment. Therefore, the overall trend in the modeling with EMC3-EIRENE matches the overall observation in the experiment that stable detachment with minimal impacts on core confinement were reached for $f_{rad} < 0.8$. Maintaining a moderate temperature reduction at the separatrix and stable operation without radiative collapse was more challenging for larger values of $f_{rad} \to 90\%$ and higher. From this comparison of experiment and modeling, an f_{rad} value between $80 - 90\%$ seems optimal to maximize dissipation and hence heat flux detachment and avoid that the radiation impacts the plasma core domain adversely. The link to the plasma core domain is discussed in the next section.

6. Steady state capability of the detached island divertor scenario

This attractive divertor scenario was held stable for up to 28 s with minimal control needs and no change in the wall conditions with respect to elevated surface temperatures, enhanced impurity production or hydrogen outgassing was seen. In figure 17, the characteristic discharge time traces of this long pulse, stable scenario with full detachment are shown. In figure 17.a, the input power P_{ECRH}, the total radiated power $P_{rad,tot}$ and the radiated power in the divertor $P_{rad,div}$ is plotted. One notices a fast ramp up to full power of $P_{ECRH} = 5.2$MW at 0.5 s. During this time, the polarization of the EC-heating was switched from secondary X-mode to secondary O-mode [32] and a stable power deposition was obtained until $t = 23.5$ s, at which one gyrotron stopped working yielding a reduction of P_{ECRH} down to 4.7 MW until the end of the discharge. At $t = 2.0$ s, a density ramp from a line integrated density $n_{e,l.i.} = 10 \times 10^{19}$ m^{-2} to $n_{e,l.i.} = 12.5 \times 10^{19}$ m^{-2} was performed as shown in figure part (c), that resulted in an increase of $P_{rad,tot}$ from 2 MW to 4.6 MW, of which 1.0 MW and 2.2 MW, respectively, were irradiated as $P_{rad,div}$. It is important to note that limited spatial resolution of the bolometer system makes the exact localization of radiation losses in the edge around the last closed flux surfaces difficult. Therefore, a larger fraction of $P_{rad,tot}$ could well be attributed to $P_{rad,div}$. This is discussed below in more detail.

With this density increase and the associated increase in the radiated power fraction f_{rad}, shown in figure part (h), from $f_{rad} = 0.4$ in the attached case to $0.85 < f_{rad} < 0.95$ in the detached phase, the heat flux detaches from the divertor surface as shown in figure part (e) by the time trace of the integrated heat flux Q_{int} to the divertor and the averaged heat flux $< q >$. Both measured heat fluxes are reduced to $30 - 40\%$ of the values during the short attached phase before 2.5 s. During this transition into detachment, the energy confinement stays constant as seen in figure part (b), where the time traces of the ion temperature $T_i(t)$, electron temperature $T_e(t)$ and of the diamagnetic energy W_{dia} are depicted. Stable conditions at $T_i = 1.5$ keV, $T_e = 2.2$ keV and $W_{dia} = 620$ kJ were demonstrated for the entire duration of the detached phase. The only noticeable small change during the 28 s long detached phase are a result of the loss of the heating power of one gyrotron. The density time traces stay constant as seen in figure part (c) and the effective charge number as a measure for the plasma purity stays constant at $Z_{eff} = 1.5$.

In the right column of subfigure in figure 17, the particle fluxes (part (f)) and the neutral pressure measurements (part (g)) are shown. The particle fluxes are quantified as before by using the ion saturation current I_{sat} from the Langmuir probe nearest to the

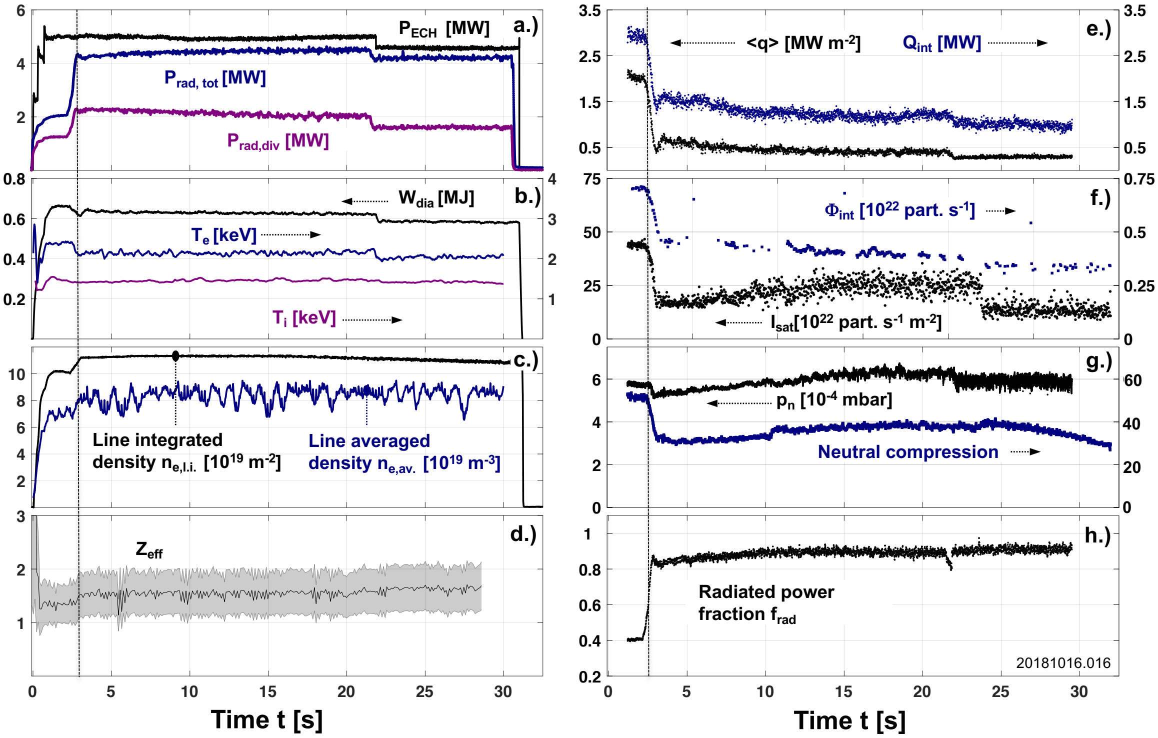

Figure 17: Stable detached discharge scenario for 28s with full detachment and stable high neutral pressures in the 10^{-4}mbar regime. Please see explanations in text for details.

strike line (black curve with axis on the left in figure part (f)). In addition, the averaged integrated recycling flux Φ_{int} on the horizontal and vertical targets of all divertor modules is shown as blue curve with axis on the right in figure part (f). Both particle flux measures are reduced to 20 % of the attached value (I_{sat}) and to 50 % of the attached value (Φ_{int}). However, for the latter value no adjusted S/XB coefficient was used. If we assume the same coefficient as used in the analysis of the slow density ramp before, Φ_{int} would be lowered by a factor 8/32 due to the reduction of S/XB from 32 in the attached phase to 8 during detachment. This systematic uncertainty from the S/XB coefficient leaves the assessment of the actual particle flux reduction open until more detailed spectroscopic studies have been conducted. However, it can be clearly seen that both heat as well as particle fluxes are reduced on a level that represents a substantial detachment and lowers heat flux and eroding particle fluxes strongly.

The detachment of this long pulse discharge goes along with significant neutral pressure build up and neutral compression. This is shown in figure 17.g. Here, the averaged divertor neutral pressure p_n in the vicinity of the entrance to the divertor chamber is shown by the black curve with axis on the left and the neutral compression ratio C_n is shown as blue time trace with axis on the right. At the transition into detachment, p_n is reduced somewhat and recovers to exceed the level of pressure seen before detachment. The neutral compression is reduced from > 50 to ≈ 40. This analysis confirms that even for the duration of 28 s heat and particle flux detachment was combined with substantial neutral pressures and significant neutral compression. The relation between this control of the neutral particle inventory and the exhaust capacity of the divertor will be discussed at the end of this paper. Over the entire duration of the detached phase the radiative power fraction f_{rad} stayed > 0.8, but well below unity. We saw no indication that this discharge scenario would turn unstable; instead, it appeared that this scenario is a steady-state operational regime.

In order to assess the scaling of this detached scenario towards steady state conditions, the scaling of the density and the divertor pressure with power was investigated, assuming that the direct relation between f_{rad} and the density as discussed before prevails. In figure 18.a, the scaling of $n_{e,l.i.}$ with input power P_{ECRH} is shown and in figure 18.b, the scaling of $\bar{p}_{n,div}$ with $n_{e,l.i.}$. To obtain this scaling, the stably detached phases for this set of discharges were used. As another sorting criterion, the applied divertor control coil current I_{CC} was used, which is embedded in both plots by the according markers and colors. Red triangle markers denote averaged densities and neutral pressures for the $I_{CC} = 0$kA case, black diamond markers are for the $I_{CC} = 1$kA cases, and green square markers stand for the $I_{CC} = 2$kA case. One case at $I_{CC} = 2.5$kA is included as blue circle marker. This analysis reveals that the density obtained scales nearly linearly with input power and similarly the averaged neutral pressures scale linearly with the density. The scaling of f_{rad} with density was discussed earlier based on figure 11.a. These findings together suggest that increased heating power at comparable external fueling levels (see

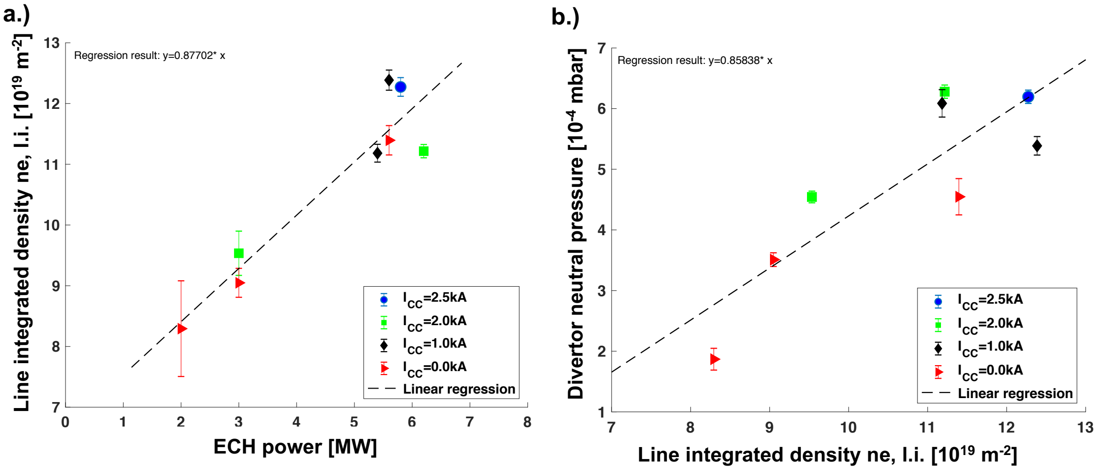

Figure 18: Scaling of $n_{e,l.i.}$ with heating power (part (a)) and of p_n with $n_{e,l.i.}$ (part (b)).The data set contains averages across the stable detached phases of various discharges with different values of divertor control coil currents I_{CC} with $0.7 < f_{rad} < 0.8$

.

next section) results in an increase of the density. Explanation of this finding requires establishing a full particle balance for these scenarios that accounts for the external, recycling and first wall particle sources, as well as the number of exhausted particles and the total number of particles in the plasma (see, for instance, the single reservoir particle balance models in [80, 81, 82]). Such an analysis is commencing presently [83] and the details of this topic are hence deferred to a later paper. The observed correlation of $n_{l.i.}(P_{ECRH})$ can possibly be linked to increased particle sourcing from the first wall with higher heating power in combination with increased fueling efficiencies. The relation between $f_{rad}(n_{l.i.})$ is, as discussed, most likely related to increased particle fluxes and increased impurity sourcing as well as increasing radiation efficiencies of C as T_e is reduced. The resulting increase in $p_n(P_{ECRH})$ and hence $p_n(f_{rad})$ includes this dependence on the line integrated density. This complex topic is subject to further analysis and maybe more experiments. An initial attempt on investigating the underlying impurity content in the island divertor is described in [84] and is being prepared for publication elsewhere.

The correlation between the level of I_{CC} and p_n is obstructed by the fact that not all discharges were operated at the optimum $f_{rad} = 0.8$. Those measurements that reside underneath the scaling but still were operated with $I_{CC} > 0$ kA featured elevated $0.9 < f_{rad} < 1$. They were found to result in a gradual decrease of p_n at this radiation level. However, a clear tendency is seen in figure 18.b that the manipulation of the island size when applying I_{CC} even at the 1kA level can increase the neutral pressure by $30 - 40\%$. This is particularly obvious at $n_{e,l.i.} = 11.5 \times 10^{19}$ m^{-3} in figure 18.b, where already at $I_{CC} = 1$ kA an increase of p_n of 50 % is indicated. However, further raising of I_{CC} did not yield further pressure increase. In general, the discharges with $I_{CC} > 0$ kA are found above the cases with no coil current at comparable densities. Importantly, as a general trend, these results show a weakly linear scaling of p_n with input power. Therefore, a further enhancement of the pressure build up capacity during detachment in the island divertor is expected as input power capacity will be increased for future campaigns.

An important aspect of the stable particle balance is an equilibrium of the amount of particles injected to fuel the detached discharge and the amount of particles pumped. This is shown in figure 19, with the divertor fueling rate in atoms/s in black and the pumped flux in atoms/s in red. On the left the 30 s these time traces are shown for the discharge discussed above and on the right, the time traces for a comparable detachment program are depicted. Overall, for both discharges a comparable level of particle source $(3 - 4.5 \times 10^{21}$ at/s) is required to establish the scenario and the particle source requirement decays while the discharge evolves into the steady state conditions. The decay rates of the particle source for both discharges is different and the reason for this is most likely found in the history of the wall condition. However, these two examples show that within the duration of the discharge, the source flux and pumped flux come

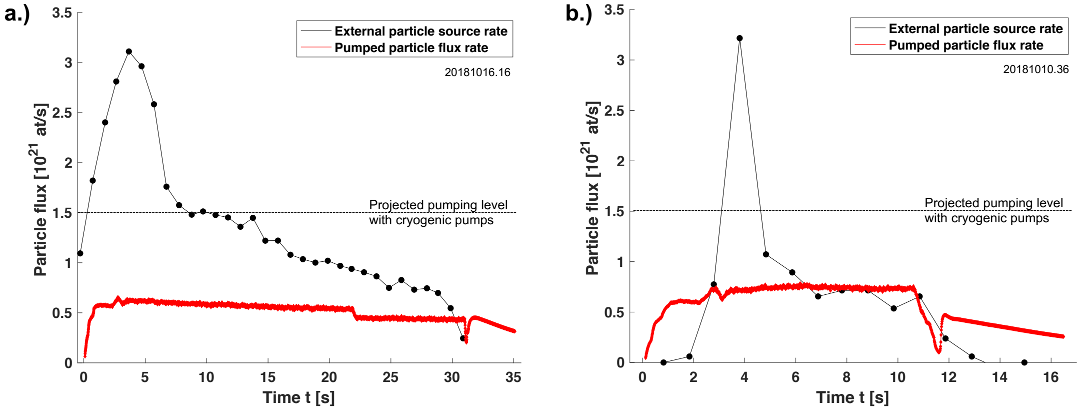

Figure 19: Time traces of particle source rates and pumped neutral particle flux rates showing that an equilibrium is obtained that is the basis for a steady state particle balance.

into an equilibrium, at least within uncertainties of the measurements. A discussion of what the actual source and sink rate numbers mean in terms of a stably pumped particle balance will follow. The black horizontal line in figure 19 (b) show the level of pumping that would be obtained for the neutral pressures achieved in these discharges with the cryogenic pumping system that will be installed for future campaigns.

The pressure levels reached in the divertor pumping domain scale favorably towards steady state particle exhaust conditions for the upcoming high-performance campaign in 2022, where the actively cooled High-Heat-Flux (HHF) divertor will be installed. In order to assess the exhaust capabilities under the neutral pressure conditions measured during detachment, the pumped flux Φ_{pump} is compared to the neutral particle flux Φ_{in} injected through gas feedback system during these discharges. The pumping was realized during the Test Divertor unit (TDU) campaign using Turbo Molecular Pumps (TMPs) with a total pumping speed of $37,500$ liter H_2 s^{-1}. With the HHF divertor, a cryo-pump will be installed which will approximately triple the pumping capacity to a total of $108,000$ liter H_2 s^{-1}. To calculate Φ_{pump}, we use the maximum pressure value of 8.0×10^{-4}mbar reached during detached plasma scenarios after the boronization and the maximal pressure before boronization, which was found to be 5.0×10^{-5}mbar. To calculate Φ_{in}, the injected gas flux from all gas injections systems at W7-X was added up. This approach utilizes the fact that the discharges were initially fueled by desorption from the wall and later were carried forward with gas injection. The initial gas balance indicates that during this phase, the density feedback system requested enough gas to over-fuel the system and the wall reservoir was absorbing particles until the end of the discharge. This means that the gas flux accounted for actually exceeds the steady state particle source requirements and represents an upper maximum.

In table 1, a comparison of the gas input and output for the detached scenarios before and after the boronization is shown. For the scenario before boronization, too low neutral pressures were reached which limits the capacity to exhaust the injected flux for steady state density conditions in these plasmas. The fueling efficiency was lower for these scenarios as seen in moderate densities for comparable resulting in even higher injected particle fluxes Φ_{in}. After the boronization, however, the necessary neutral flux was balanced by the exhausted flux due to the strong increase of the neutral pressure during full thermal detachment including reduced particle fluxes. Because the pumping capacity will even further increase in the HHF divertor due to the cryo-pump, steady state pumping is very likely possible for the high-performance, steady state regime, assuming the injected gas flux will fuel at least as efficient as in the conditions of the detached plasmas in the past campaign.

Scenario	**Value**	**TMP only in TDU**	**with cryo-pump in HHF**
Post-boronization	Φ_{pump}	5.2×10^{20} H_2/s	1.4×10^{21} H_2/s
	Φ_{in}	$5.0 - 8.0 \times 10^{20}$ H_2/s	$5.0 - 8.0 \times 10^{20}$ H_2/s assumed
Pre-boronization	Φ_{pump}	9.0×10^{19} H_2/s	2.7×10^{20} H_2/s
	Φ_{in}	$2.2 - 20.0 \times 10^{20}$ H_2/s	does not scale

Table 1: Overview of particle exhaust capabilities for the pre- and post-boronization scenarios calculated for the exhaust capacity with TMP only for the Test Divertor unit (TDU) compared to the the High-Heat-Flux (HHF) divertor with cryo-pump.

7. Summary and conclusion

A stable, thermally fully detached island divertor regime has been demonstrated in the island divertor at Wendelstein 7-X. This maintains heat fluxes to the divertor target plates on technically feasible levels throughout the detached discharges. Particle fluxes are reduced substantially to reduce heat deposition by recombination in the target material and material sputtering. This is accomplished simultaneously with an neutral pressure and neutral compression level that scales favorably towards steady state particle exhaust for the upcoming High-Heat-Flux (HHF) divertor campaign. This scenario is based on sufficient radiative power dissipation by carbon as intrinsic impurity. Stable detached plasma conditions were obtained at radiative power fractions of 80%, which are accessible for a broad range of ECH power levels between $P_{ECRH} = 3$MW up to the maximum, stably available power during the campaign of $P_{ECRH} = 6.2$MW. A linear density scaling with P_{ECRH} was found for the detached phases of these discharges, which resulted in a linear scaling of the accomplished neutral pressures with P_{ECRH} through density. Even without any further enhancement of the heating power capacities of W7-X, this regime scales favorably to steady state particle exhaust conditions. The neutral pressures reached enabled to exhaust the amount of injected particles to fuel the discharge in steady state with the pumping scheme based on Turbo Molecular

Pumps (TMPs) only. The cryogenic pump, which will be installed for the HHF divertor setup, will provide further headroom to expect a stable and steady state particle exhaust regime. Further particle sources could be tolerated if required for instance for density profile shaping by pellet or neutral beam injection. A first long pulse demonstration for up to 28s was accomplished in the past campaign, in which full thermal detachment with reduced particle fluxes at sufficient neutral pressure was held stable, only limited by the capacity of the ECH heating system and eventually input energy limits.

A key element in this promising island divertor scenario is the dependence on the sufficient amount of radiators that radiate at the right temperature to locate the impurities and the radiation in some layer around the island divertor domain. However, the exact location of the dominant radiative losses cannot be measured presently and is a matter of further analysis aided by 3D modeling efforts. The analysis presented supports a strong localization of the radiation just inside of the island separatrix which relies on a fine balance of radiative cooling and the ionization and impurity trapping in the divertor. Detailed analysis of the divertor impurity content and its capacity to retain the impurities will be addressed in future papers. But towards the reactor perspective, where almost certainly different material choices will be made, it will be essential to investigate the detachment behavior with such impurities. Seeding of impurities, in particular Nitrogen (N), is a candidate to substitute the functionality of carbon as studied in detail already for tokamak divertor solutions (see e.g. [85, 86, 87]) and was also studied intensively at LHD [88]. It was shown in [67], that the transition into detachment can be induced by N seeding for the island divertor at W7-X. The integration of this finding into the stable detached regime discussed here and the extrapolation of this island divertor regime towards reactors with different PFMC materials remains a future challenge.

Acknowledgements This work was funded by the U.S. Department of Energy under grant DE-SC00014210 and DE-SC00013911. The publisher, by accepting the article for publication acknowledges, that the United States Government retains a non-exclusive, paid-up, irrevocable, world-wide license to publish or reproduce the published form of this manuscript, or allow others to do so, for United States Government purposes. This work has been carried out within the framework of the EUROfusion Consortium with funding from the Euratom research and training program 2014-2018 and 2019-2020 under grant agreement No 633053. The views and opinions expressed herein do not necessarily reflect those of the European Commission. The main author of this paper wants to express his sincere gratitude to the entire W7-X team for the support in compiling this document, the data contained and the invited talk on the 2019 EPS-DPP conference in Milan, Italy.

[1] Lyman Spitzer. The stellarator concept. *The Physics of Fluids*, 1(4):253–264, 1958.
[2] A.H. Boozer. What is a stellarator? *Physics of Plasmas*, 5(5):1647–1655, 1998.

[3] A.H Boozer. Stellarators and the path from ITER to DEMO. *Plasma Physics and Controlled Fusion*, 50(12):124005, 2008.

[4] H. Renner, J. Boscary, V. Erckmann, H. Greuner, H. Grote, J. Sapper, E. Speth, F. Wesner, M. Wanner, and W7-X Team. The capabilities of steady state operation at the stellarator W7-X with emphasis on divertor design. *Nuclear Fusion*, 40(6):1083, 2000.

[5] R König, P Grigull, K McCormick, Y Feng, J Kisslinger, A Komori, S Masuzaki, K Matsuoka, T Obiki, N Ohyabu, H Renner, F Sardei, F Wagner, and A Werner. The divertor program in stellarators. *Plasma Physics and Controlled Fusion*, 44(11):2365, 2002.

[6] H.-S. Bosch, R.C. Wolf, T. Andreeva, J. Baldzuhn, D. Birus, T. Bluhm, T. Bräuer, H. Braune, V. Bykov, A. Cardella, F. Durodié, M. Endler, V. Erckmann, G. Gantenbein, D. Hartmann, D. Hathiramani, P. Heimann, B. Heinemann, C. Hennig, M. Hirsch, D. Holtum, J. Jagielski, J. Jelonnek, W. Kasparek, T. Klinger, R. König, P. Kornejew, H. Kroiss, J.G. Krom, G. Kühner, H. Laqua, H.P. Laqua, C. Lechte, M. Lewerentz, J. Maier, P. McNeely, A. Messiaen, G. Michel, J. Ongena, A. Peacock, T.S. Pedersen, R. Riedl, H. Riemann, P. Rong, N. Rust, J. Schacht, F. Schauer, R. Schroeder, B. Schweer, A. Spring, A. Stäbler, M. Thumm, Y. Turkin, L. Wegener, A. Werner, D. Zhang, M. Zilker, T. Akijama, R. Alzbutas, E. Ascasibar, M. Balden, M. Banduch, Ch. Baylard, W. Behr, C. Beidler, A. Benndorf, T. Bergmann, C. Biedermann, B. Bieg, W. Biel, M. Borchardt, G. Borowitz, V. Borsuk, S. Bozhenkov, R. Brakel, H. Brand, T. Brown, B. Brucker, R. Burhenn, K.-P. Buscher, C. Caldwell-Nichols, A. Cappa, A. Cardella, A. Carls, P. Carvalho, Ł. Ciupiński, M. Cole, J. Collienne, A. Czarnecka, G. Czymek, G. Dammertz, C.P. Dhard, V.I. Davydenko, A. Dinklage, M. Drevlak, S. Drotziger, A. Dudek, P. Dumortier, G. Dundulis, P.v. Eeten, K. Egorov, T. Estrada, H. Faugel, J. Fellinger, Y. Feng, H. Fernandes, W.H. Fietz, W. Figacz, F. Fischer, J. Fontdecaba, A. Freund, T. Funaba, H. Fünfgelder, A. Galkowski, D. Gates, L. Giannone, J.M. García Regaña, J. Geiger, S. Geißler, H. Greuner, M. Grahl, S. Groß, A. Grosman, H. Grote, O. Grulke, M. Haas, L. Haiduk, H.-J. Hartfuß, J.H. Harris, D. Haus, B. Hein, P. Heitzenroeder, P. Helander, R. Heller, C. Hidalgo, D. Hildebrandt, H. Höhnle, A. Holtz, E. Holzhauer, R. Holzthüm, A. Huber, H. Hunger, F. Hurd, M. Ihrke, S. Illy, A. Ivanov, S. Jablonski, N. Jaksic, M. Jakubowski, R. Jaspers, H. Jensen, H. Jenzsch, J. Kacmarczyk, T. Kaliatk, J. Kallmeyer, U. Kamionka, R. Karaleviciu, S. Kern, M. Keunecke, R. Kleiber, J. Knauer, R. Koch, G. Kocsis, A. Könies, M. Köppen, R. Koslowski, J. Koshurinov, A. Krämer-Flecken, R. Krampitz, Y. Kravtsov, M. Krychowiak, G. Krzesinski, I. Ksiazek, Fr. Kubkowska, A. Kus, S. Langish, R. Laube, M. Laux, S. Lazerson, M. Lennartz, C. Li, R. Lietzow, A. Lohs, A. Lorenz, F. Louche, L. Lubyako, A. Lumsdaine, A. Lyssoivan, H. Maaßberg, P. Marek, C. Martens, N. Marushchenko, M. Mayer, B. Mendelevitch, Ph. Mertens, D. Mikkelsen, A. Mishchenko, B. Missal, T. Mizuuchi, H. Modrow, T. Mönnich, T. Morizaki, S. Murakami, F. Musielok, M. Nagel, D. Naujoks, H. Neilson, O. Neubauer, U. Neuner, R. Nocentini, J.-M. Noterdaeme, C. Nührenberg, S. Obermayer, G. Offermanns, H. Oosterbeek, M. Otte, A. Panin, M. Pap, S. Paquay, E. Pasch, X. Peng, S. Petrov, D. Pilopp, H. Pirsch, B. Plaum, F. Pompon, M. Povilaitis, J. Preinhaelter, O. Prinz, F. Purps, T. Rajna, S. Récsei, A. Reiman, D. Reiter, J. Remmel, S. Renard, V. Rhode, J. Riemann, S. Rimkevicius, K. Riße, A. Rodatos, I. Rodin, M. Romé, H.-J. Roscher, K. Rummel, Th. Rummel, A. Runov, L. Ryc, J. Sachtleben, A. Samartsev, M. Sanchez, F. Sano, A. Scarabosio, M. Schmid, H. Schmitz, O. Schmitz, M. Schneider, W. Schneider, L. Scheibl, M. Scholz, G. Schröder, M. Schröder, J. Schruff, H. Schumacher, I.V. Shikhovtsev, M. Shoji, G. Siegl, J. Skodzik, M. Smirnow, E. Speth, D.A. Spong, R. Stadler, Z. Sulek, V. Szabó, T. Szabolics, T. Szetefi, Z. Szökefalvi-Nagy, A. Tereshchenko, H. Thomsen, M. Thumm, D. Timmermann, H. Tittes, K. Toi, M. Tournianski, U.v. Toussaint, J. Tretter, S. Tulipán, P. Turba, R. Uhlemann, J. Urban, E. Urbonavicius, P. Urlings, S. Valet, D. Van Eester, M. Van Schoor, M. Vervier, H. Viebke, R. Vilbrandt, M. Vrancken, T. Wauters, M. Weissgerber, E. Weiß, A. Weller, J. Wendorf, U. Wenzel, T. Windisch, E. Winkler, M. Winkler, J. Wolowski, J. Wolters, G. Wrochna, P. Xanthopoulos, H. Yamada, M. Yokoyama, D. Zacharias, J. Zajac, G. Zangl, M. Zarnstorff, H. Zeplien,

S. Zoletnik, and M. Zuin. Technical challenges in the construction of the steady-state stellarator wendelstein 7-x. *Nuclear Fusion*, 53(12):126001, 2013.

[7] J Geiger, C D Beidler, Y Feng, H Maaßberg, N B Marushchenko, and Y Turkin. Physics in the magnetic configuration space of w7-x. *Plasma Physics and Controlled Fusion*, 57(1):014004, 2015.

[8] D.A. Gates, A.H. Boozer, T. Brown, J. Breslau, D. Curreli, M. Landreman, S.A. Lazerson, J. Lore, H. Mynick, G.H. Neilson, N. Pomphrey, P. Xanthopoulos, and A. Zolfaghari. Recent advances in stellarator optimization. *Nuclear Fusion*, 57(12):126064, oct 2017.

[9] S. Masuzaki, M. Kobayashi, T. Morisaki, N. Ohyabu, A. Komori, and Y. Feng. Investigation on the influence of plasma properties and SOL transport on the particle flux profiles on divertor plates in the large helical device. *Journal of Nuclear Materials*, 390–391(0):286 – 289, 2009. Proceedings of the 18th International Conference on Plasma-Surface Interactions in Controlled Fusion Device Proceedings of the 18th International Conference on Plasma-Surface Interactions in Controlled Fusion Device.

[10] S. Masuzaki, M. Shoji, M. Tokitani, T. Murase, M. Kobayashi, T. Morisaki, H. Yonezu, R. Sakamoto, H. Yamada, and A. Komori. Design and installation of the closed helical divertor in LHD. *Fusion Engineering and Design*, 85(6):940 – 945, 2010.

[11] T. Morisaki, S. Masuzaki, M. Kobayashi, M. Shoji, J. Miyazawa, R. Sakamoto, G. Motojima, M. Goto, H. Funaba, H. Tanaka, K. Tanaka, I. Yamada, S. Ohdachi, H. Yamada, A. Komori, and the LHD Experiment Group. Initial experiments towards edge plasma control with a closed helical divertor in LHD. *Nuclear Fusion*, 53(6):063014, 2013.

[12] G. Motojima, S. Masuzaki, H. Tanaka, T. Morisaki, R. Sakamoto, T. Murase, Y. Tsuchibushi, M. Kobayashi, O. Schmitz, M. Shoji, M. Tokitani, H. Yamada, and Y. Takeiri and. Establishment of a low recycling state with full density control by active pumping of the closed helical divertor at LHD. *Nuclear Fusion*, 58(1):014005, nov 2017.

[13] G. Motojima, S. Masuzaki, T. Morisaki, H. Tanaka, R. Sakamoto, T. Murase, S. Oliver, M. Kobayashi, M. Shoji, M. Tokitani, Y. Tsuchibushi, H. Yamada, and Y. Takeiri and. New approach to the control of particle recycling using divertor pumping in the Large Helical Device. *Nuclear Fusion*, 59(8):086022, jun 2019.

[14] Allen H. Boozer. Stellarator design. *Journal of Plasma Physics*, 81(6):515810606, 2015.

[15] E. Strumberger. Stochastic magnetic field structure in the edge region of w7-x. *Contributions to Plasma Physics*, 38(1-2):106–111, 1998.

[16] A. Bader, D.T. Anderson, C.C. Hegna, Y. Feng, J.D. Lore, and J.N. Talmadge. Simulations of edge configurations in quasi-helically symmetric geometry using EMC3–EIRENE. *Nuclear Fusion*, 53(11):113036, 2013.

[17] A. Bader, A. H. Boozer, C. C. Hegna, S. A. Lazerson, and J. C. Schmitt. Hsx as an example of a resilient non-resonant divertor. *Physics of Plasmas*, 24(3):032506, 2017.

[18] A R Akerson, A Bader, C C Hegna, O Schmitz, L A Stephey, D T Anderson, F S B Anderson, and K M Likin. Three-dimensional scrape off layer transport in the helically symmetric experiment HSX. *Plasma Physics and Controlled Fusion*, 58(8):084002, 2016.

[19] Y. Feng, F. Sardei, P. Grigull, K. McCormick, J. Kisslinger, and D. Reiter. Physics of island divertors as highlighted by the example of W7-AS. *Nuclear Fusion*, 46(8):807, 2006.

[20] Y. Feng, C.D. Beidler, J. Geiger, P. Helander, H. Hölbe, H. Maassberg, Y. Turkin, and D. Reiter and. On the W7-X divertor performance under detached conditions. *Nuclear Fusion*, 56(12):126011, sep 2016.

[21] P Grigull, K McCormick, J Baldzuhn, R Burhenn, R Brakel, H Ehmler, Y Feng, F Gadelmeier, L Giannone, D Hartmann, D Hildebrandt, M Hirsch, R Jaenicke, J Kisslinger, J Knauer, R König, G Kühner, H Laqua, D Naujoks, H Niedermeyer, N Ramasubramanian, N Rust, F Sardei, F Wagner, A Weller, U Wenzel, and the W7-AS Team. First island divertor experiments on the W7-AS stellarator. *Plasma Physics and Controlled Fusion*, 43(12A):A175, 2001.

[22] H Renner, J Boscary, H Greuner, H Grote, F W Hoffmann, J Kisslinger, E Strumberger, and B Mendelevitch. Divertor concept for the W7-X stellarator and mode of operation. *Plasma Physics and Controlled Fusion*, 44(6):1005, 2002.

[23] J. Geiger, C.D. Beidler, M. Drevlak, H. Maaßberg, C. Nührenberg, Y. Suzuki, and Yu. Turkin. Effects of Net Currents on the Magnetic Configuration of W7-X. *Contributions to Plasma Physics*, 50(8):770–774, 2010.

[24] H Renner, J Boscary, V Erckmann, H Greuner, H Grote, J Sapper, E Speth, F Wesner, M Wanner, and W7-X Team. The capabilities of steady state operation at the stellarator W7-X with emphasis on divertor design. *Nuclear Fusion*, 40(6):1083–1093, jun 2000.

[25] H Renner, J Boscary, H Greuner, H Grote, F W Hoffmann, J Kisslinger, E Strumberger, and B Mendelevitch. Divertor concept for the W7-X stellarator and mode of operation. *Plasma Physics and Controlled Fusion*, 44(6):1005–1019, may 2002.

[26] T. Sunn Pedersen, R. König, M. Jakubowski, M. Krychowiak, D. Gradic, C. Killer, H. Niemann, T. Szepesi, U. Wenzel, A. Ali, G. Anda, J. Baldzuhn, T. Barbui, C. Biedermann, B.D. Blackwell, H.-S. Bosch, S. Bozhenkov, R. Brakel, S. Brezinsek, J. Cai, B. Cannas, J.W. Coenen, J. Cosfeld, A. Dinklage, T. Dittmar, P. Drewelow, P. Drews, D. Dunai, F. Effenberg, M. Endler, Y. Feng, J. Fellinger, O. Ford, H. Frerichs, G. Fuchert, Y. Gao, J. Geiger, A. Goriaev, K. Hammond, J. Harris, D. Hathiramani, M. Henkel, Ye.O. Kazakov, A. Kirschner, A. Knieps, M. Kobayashi, G. Kocsis, P. Kornejew, T. Kremeyer, S. Lazerzon, A. LeViness, C. Li, Y. Li, Y. Liang, S. Liu, J. Lore, S. Masuzaki, V. Moncada, O. Neubauer, T.T. Ngo, J. Oelmann, M. Otte, V. Perseo, F. Pisano, A. Puig Sitjes, M. Rack, M. Rasinski, J. Romazanov, L. Rudischhauser, G. Schlisio, J.C. Schmitt, O. Schmitz, B. Schweer, S. Sereda, M. Sleczka, Y. Suzuki, M. Vecsei, E. Wang, T. Wauters, S. Wiesen, V. Winters, G.A. Wurden, D. Zhang, and S. Zoletnik and. First divertor physics studies in Wendelstein 7-X. *Nuclear Fusion*, 59(9):096014, jul 2019.

[27] D. Sharma, Y. Feng, F. Sardei, J. Kisslinger, H. Grote, P. Grigull, and H. Renner. Pumping capability and particle balance in W7-X: a self-consistent 3D study. *Journal of Nuclear Materials*, 337–339(0):471 – 474, 2005.

[28] D Sharma, Y Feng, F Sardei, and D Reiter. Three-dimensional Monte Carlo simulations of W7-X plasma transport: density control and particle balance in steady-state operations. *Nuclear Fusion*, 45(8):825–836, jul 2005.

[29] D. Sharma, Y. Feng, and F. Sardei. A 3D monte-carlo study of the W7-X island divertor transport for different magnetic configurations. *Nuclear Fusion*, 46(4):S127, 2006.

[30] Thomas Sunn Pedersen, Ralf König, Maciej Krychowiak, Marcin Jakubowski, Jürgen Baldzuhn, Sergey Bozhenkov, Golo Fuchert, Andreas Langenberg, Holger Niemann, Daihong Zhang, Kian Rahbarnia, Hans-Stephan Bosch, Yevgen Kazakov, Sebastijan Brezinsek, Yu Gao, and Novimir Pablant and. First results from divertor operation in Wendelstein 7-X. *Plasma Physics and Controlled Fusion*, 61(1):014035, nov 2018.

[31] T. Klinger, T. Andreeva, S. Bozhenkov, C. Brandt, R. Burhenn, B. Buttenschön, G. Fuchert, B. Geiger, O. Grulke, H.P. Laqua, N. Pablant, K. Rahbarnia, T. Stange, A. von Stechow, N. Tamura, H. Thomsen, Y. Turkin, T. Wegner, I. Abramovic, S. Äkäslompolo, J. Alcuson, P. Aleynikov, K. Aleynikova, A. Ali, A. Alonso, G. Anda, E. Ascasibar, J.P. Bähner, S.G. Baek, M. Balden, J. Baldzuhn, M. Banduch, T. Barbui, W. Behr, C. Beidler, A. Benndorf, C. Biedermann, W. Biel, B. Blackwell, E. Blanco, M. Blatzheim, S. Ballinger, T. Bluhm, D. Böckenhoff, B. Böswirth, L.-G. Böttger, M. Borchardt, V. Borsuk, J. Boscary, H.-S. Bosch, M. Beurskens, R. Brakel, H. Brand, T. Bräuer, H. Braune, S. Brezinsek, K.-J. Brunner, R. Bussiahn, V. Bykov, J. Cai, I. Calvo, B. Cannas, A. Cappa, A. Carls, D. Carralero, L. Carraro, B. Carvalho, F. Castejon, A. Charl, N. Chaudhary, D. Chauvin, F. Chernyshev, M. Cianciosa, R. Citarella, G. Claps, J. Coenen, M. Cole, M.J. Cole, F. Cordella, G. Cseh, A. Czarnecka, K. Czerski, M. Czerwinski, G. Czymek, A. da Molin, A. da Silva, H. Damm, A. de la Pena, S. Degenkolbe, C.P. Dhard, M. Dibon, A. Dinklage, T. Dittmar, M. Drevlak, P. Drewelow, P. Drews, F. Durodie, E. Edlund, P. van Eeten, F. Effenberg, G. Ehrke,

S. Elgeti, M. Endler, D. Ennis, H. Esteban, T. Estrada, J. Fellinger, Y. Feng, E. Flom, H. Fernandes, W.H. Fietz, W. Figacz, J. Fontdecaba, O. Ford, T. Fornal, H. Frerichs, A. Freund, T. Funaba, A. Galkowski, G. Gantenbein, Y. Gao, J. García Regaña, D. Gates, J. Geiger, V. Giannella, A. Gogoleva, B. Goncalves, A. Goriaev, D. Gradic, M. Grahl, J. Green, H. Greuner, A. Grosman, H. Grote, M. Gruca, C. Guerard, P. Hacker, X. Han, J.H. Harris, D. Hartmann, D. Hathiramani, B. Hein, B. Heinemann, P. Helander, S. Henneberg, M. Henkel, J. Hernandez Sanchez, C. Hidalgo, M. Hirsch, K.P. Hollfeld, U. Höfel, A. Hölting, D. Höschen, M. Houry, J. Howard, X. Huang, Z. Huang, M. Hubeny, M. Huber, H. Hunger, K. Ida, T. Ilkei, S. Illy, B. Israeli, S. Jablonski, M. Jakubowski, J. Jelonnek, H. Jenzsch, T. Jesche, M. Jia, P. Junghanns, J. Kacmarczyk, J.-P. Kallmeyer, U. Kamionka, H. Kasahara, W. Kasparek, Y.O. Kazakov, N. Kenmochi, C. Killer, A. Kirschner, R. Kleiber, J. Knauer, M. Knaup, A. Knieps, T. Kobarg, G. Kocsis, F. Köchl, Y. Kolesnichenko, A. Könies, R. König, P. Kornejew, J.-P. Koschinsky, F. Köster, M. Krämer, R. Krampitz, A. Krämer-Flecken, N. Krawczyk, T. Kremeyer, J. Krom, M. Krychowiak, I. Ksiazek, M. Kubkowska, G. Kühner, T. Kurki-Suonio, P.A. Kurz, S. Kwak, M. Landreman, P. Lang, R. Lang, A. Langenberg, S. Langish, H. Laqua, R. Laube, S. Lazerson, C. Lechte, M. Lennartz, W. Leonhardt, C. Li, C. Li, Y. Li, Y. Liang, C. Linsmeier, S. Liu, J.-F. Lobsien, D. Loesser, J. Loizu Cisquella, J. Lore, A. Lorenz, M. Losert, A. Lücke, A. Lumsdaine, V. Lutsenko, H. Maaßberg, O. Marchuk, J.H. Matthew, S. Marsen, M. Marushchenko, S. Masuzaki, D. Maurer, M. Mayer, K. McCarthy, P. McNeely, A. Meier, D. Mellein, B. Mendelevitch, P. Mertens, D. Mikkelsen, A. Mishchenko, B. Missal, J. Mittelstaedt, T. Mizuuchi, A. Mollen, V. Moncada, T. Mönnich, T. Morisaki, D. Moseev, S. Murakami, G. Náfrádi, M. Nagel, D. Naujoks, H. Neilson, R. Neu, O. Neubauer, U. Neuner, T. Ngo, D. Nicolai, S.K. Nielsen, H. Niemann, T. Nishizawa, R. Nocentini, C. Nührenberg, J. Nührenberg, S. Obermayer, G. Offermanns, K. Ogawa, J. Ölmanns, J. Ongena, J.W. Oosterbeek, G. Orozco, M. Otte, L. Pacios Rodriguez, N. Panadero, N. Panadero Alvarez, D. Papenfuß, S. Paqay, E. Pasch, A. Pavone, E. Pawelec, T.S. Pedersen, G. Pelka, V. Perseo, B. Peterson, D. Pilopp, S. Pingel, F. Pisano, B. Plaum, G. Plunk, P. Pölöskei, M. Porkolab, J. Proll, M.-E. Puiatti, A. Puig Sitjes, F. Purps, M. Rack, S. Récsei, A. Reiman, F. Reimold, D. Reiter, F. Remppel, S. Renard, R. Riedl, J. Riemann, K. Risse, V. Rohde, H. Röhlinger, M. Romé, D. Rondeshagen, P. Rong, B. Roth, L. Rudischhauser, K. Rummel, T. Rummel, A. Runov, N. Rust, L. Ryc, S. Ryosuke, R. Sakamoto, M. Salewski, A. Samartsev, E. Sanchez, F. Sano, S. Satake, J. Schacht, G. Satheeswaran, F. Schauer, T. Scherer, J. Schilling, A. Schlaich, G. Schlisio, F. Schluck, K.-H. Schlüter, J. Schmitt, H. Schmitz, O. Schmitz, S. Schmuck, M. Schneider, W. Schneider, P. Scholz, R. Schrittwieser, M. Schröder, T. Schröder, R. Schroeder, H. Schumacher, B. Schweer, E. Scott, S. Sereda, B. Shanahan, M. Sibilia, P. Sinha, S. Sipliä, C. Slaby, M. Sleczka, H. Smith, W. Spiess, D.A. Spong, A. Spring, R. Stadler, M. Stejner, L. Stephey, U. Stridde, C. Suzuki, J. Svensson, V. Szabó, T. Szabolics, T. Szepesi, Z. Szökefalvi-Nagy, A. Tancetti, J. Terry, J. Thomas, M. Thumm, J.M. Travere, P. Traverso, J. Tretter, H. Trimino Mora, H. Tsuchiya, T. Tsujimura, S. Tulipán, B. Unterberg, I. Vakulchyk, S. Valet, L. Vano, B. van Milligen, A.J. van Vuuren, L. Vela, J.-L. Velasco, M. Vergote, M. Vervier, N. Vianello, H. Viebke, R. Vilbrandt, A. Vorköper, S. Wadle, F. Wagner, E. Wang, N. Wang, Z. Wang, F. Warmer, T. Wauters, L. Wegener, J. Weggen, Y. Wei, G. Weir, J. Wendorf, U. Wenzel, A. Werner, A. White, B. Wiegel, F. Wilde, T. Windisch, M. Winkler, A. Winter, V. Winters, S. Wolf, R.C. Wolf, A. Wright, G. Wurden, P. Xanthopoulos, H. Yamada, I. Yamada, R. Yasuhara, M. Yokoyama, M. Zanini, M. Zarnstorff, A. Zeitler, D. Zhang, H. Zhang, J. Zhu, M. Zilker, A. Zocco, S. Zoletnik, and M. Zuin. Overview of first Wendelstein 7-X high-performance operation. *Nuclear Fusion*, 59(11):112004, jun 2019.

[32] R C Wolf, S Bozhenkov, A Dinklage, G Fuchert, Y O Kazakov, H P Laqua, S Marsen, N B Marushchenko, T Stange, M Zanini, I Abramovic, A Alonso, J Baldzuhn, M Beurskens, C D Beidler, H Braune, K J Brunner, N Chaudhary, H Damm, P Drewelow, G Gantenbein, Yu Gao, J Geiger, M Hirsch, U Höfel, M Jakubowski, J Jelonnek, T Jensen, W Kasparek, J Knauer,

S B Korsholm, A Langenberg, C Lechte, F Leipold, H Trimino Mora, U Neuner, S K Nielsen, D Moseev, H Oosterbeek, N Pablant, E Pasch, B Plaum, T Sunn Pedersen, A Puig Sitjes, K Rahbarnia, J Rasmussen, M Salewski, J Schilling, E Scott, M Stejner, H Thomsen, M Thumm, Y Turkin, and F Wilde and. Electron-cyclotron-resonance heating in Wendelstein 7-X: A versatile heating and current-drive method and a tool for in-depth physics studies. *Plasma Physics and Controlled Fusion*, 61(1):014037, nov 2018.

[33] F Warmer, C D Beidler, A Dinklage, and R Wolf and. From W7-X to a HELIAS fusion power plant: motivation and options for an intermediate-step burning-plasma stellarator. *Plasma Physics and Controlled Fusion*, 58(7):074006, jun 2016.

[34] R.A. Pitts, X. Bonnin, F. Escourbiac, H. Frerichs, J.P. Gunn, T. Hirai, A.S. Kukushkin, E. Kaveeva, M.A. Miller, D. Moulton, V. Rozhansky, I. Senichenkov, E. Sytova, O. Schmitz, P.C. Stangeby, G. De Temmerman, I. Veselova, and S. Wiesen. Physics basis for the first ITER tungsten divertor. *Nuclear Materials and Energy*, 20:100696, 2019.

[35] D. Reiter, G.H. Wolf, and H. Kever. Burn condition, helium particle confinement and exhaust efficiency. *Nuclear Fusion*, 30(10):2141, 1990.

[36] M. Krychowiak, A. Adnan, A. Alonso, T. Andreeva, J. Baldzuhn, T. Barbui, M. Beurskens, W. Biel, C. Biedermann, B. D. Blackwell, H. S. Bosch, S. Bozhenkov, R. Brakel, T. Braeuer, B. Brotas de Carvalho, R. Burhenn, B. Buttenschoen, A. Cappa, G. Cseh, A. Czarnecka, A. Dinklage, P. Drews, A. Dzikowicka, F. Effenberg, M. Endler, V. Erckmann, T. Estrada, O. Ford, T. Fornal, H. Frerichs, G. Fuchert, J. Geiger, O. Grulke, J. H. Harris, H. J. Hartfuss, D. Hartmann, D. Hathiramani, M. Hirsch, U. Hoefel, S. Jablonski, M. W. Jakubowski, J. Kaczmarczyk, T. Klinger, S. Klose, J. Knauer, G. Kocsis, R. König, P. Kornejew, A. Krämer-Flecken, N. Krawczyk, T. Kremeyer, I. Ksiazek, M. Kubkowska, A. Langenberg, H. P. Laqua, M. Laux, S. Lazerson, Y. Liang, S. C. Liu, A. Lorenz, A. O. Marchuk, S. Marsen, V. Moncada, D. Naujoks, H. Neilson, O. Neubauer, U. Neuner, H. Niemann, J. W. Oosterbeek, M. Otte, N. Pablant, E. Pasch, T. Sunn Pedersen, F. Pisano, K. Rahbarnia, L. Ryc, O. Schmitz, S. Schmuck, W. Schneider, T. Schroeder, H. Schuhmacher, B. Schweer, B. Standley, T. Stange, L. Stephey, J. Svensson, T. Szabolics, T. Szepesi, H. Thomsen, J.-M. Travere, H. Trimino Mora, H. Tsuchiya, G. M. Weir, U. Wenzel, A. Werner, B. Wiegel, T. Windisch, R. Wolf, G. A. Wurden, D. Zhang, A. Zimbal, and S. Zoletnik. Overview of diagnostic performance and results for the first operation phase in Wendelstein 7-X. *Review of Scientific Instruments*, 87(11):11D304, 2016.

[37] A.S. Kukushkin, H.D. Pacher, V. Kotov, G.W. Pacher, and D. Reiter. Finalizing the ITER divertor design: The key role of SOLPS modeling. *Fusion Engineering and Design*, 86(12):2865 – 2873, 2011.

[38] S.I. Krasheninnikov, A.S. Kukushkin, A.A. Pshenov, A.I. Smolyakov, and Yanzeng Zhang. Stability of divertor detachment. *Nuclear Materials and Energy*, 12:1061 – 1066, 2017.

[39] A W Leonard. Plasma detachment in divertor tokamaks. *Plasma Physics and Controlled Fusion*, 60(4):044001, feb 2018.

[40] P.C. Stangeby and Chaofeng Sang. Strong correlation between D2 density and electron temperature at the target of divertors found in SOLPS analysis. *Nuclear Fusion*, 57(5):056007, mar 2017.

[41] K Borrass and G Janeschitz. Estimation of the maximum divertor radiative fraction in the presence of a neutral cushion. *Nuclear Fusion*, 34(9):1203–1211, sep 1994.

[42] P.C Stangeby. Can detached divertor plasmas be explained as self-sustained gas targets? *Nuclear Fusion*, 33(11):1695–1705, nov 1993.

[43] G.M. McCracken and P.E. Stott. Plasma-surface interactions in tokamaks. *Nuclear Fusion*, 19(7):889–981, jul 1979.

[44] C S Pitcher and P C Stangeby. Experimental divertor physics. *Plasma Physics and Controlled Fusion*, 39(6):779–930, jun 1997.

[45] Peter C. Stangeby. *The Plasma Boundary of Magnetic Fusion Devices*. Institute of Physics Publishing, 2000.

[46] P.C. Stangeby and A.W. Leonard. Obtaining reactor-relevant divertor conditions in tokamaks. *Nuclear Fusion*, 51(6):063001, 2011. Exported from https://app.dimensions.ai on 2019/02/28.

[47] A. Loarte, B. Lipschultz, A.S. Kukushkin, G.F. Matthews, P.C. Stangeby, N. Asakura, G.F. Counsell, G. Federici, A. Kallenbach, K. Krieger, A. Mahdavi, V. Philipps, D. Reiter, J. Roth, J. Strachan, D. Whyte, R. Doerner, T. Eich, W. Fundamenski, A. Herrmann, M. Fenstermacher, P. Ghendrih, M. Groth, A. Kirschner, S. Konoshima, B. LaBombard, P. Lang, A.W. Leonard, P. Monier-Garbet, R. Neu, H. Pacher, B. Pegourie, R.A. Pitts, S. Takamura, J. Terry, E. Tsitrone, the ITPA Scrape-off Layer, and Divertor Physics Topical Group. Chapter 4: Power and particle control. *Nuclear Fusion*, 47(6):S203, 2007.

[48] Y. Feng, T. Lunt, A. Kukushkin, M. Becoulet, T. Casper, T.E. Evans, H. Frerichs, A. Loarte, R. Pitts, D. Reiter, and O. Schmitz. EMC3-Eirene/SOLPS4.3 comparison for ITER. In *European Conference Abstracts*, volume 35G, 2011. Poster contribution P1.071 on the EPS Conference on Plasma Physics 2011, Strasbourg, France.

[49] M. Kobayashi, Y. Xu, K. Ida, Y. Corre, Y. Feng, O. Schmitz, H. Frerichs, F.L. Tabares, T.E. Evans, J.W. Coenen, Y. Liang, A. Bader, K. Itoh, H. Yamada, Ph. Ghendrih, G. Ciraolo, D. Tafalla, A. Lopez-Fraguas, H.Y. Guo, Z.Y. Cui, D. Reiter, N. Asakura, U. Wenzel, S. Morita, N. Ohno, B.J. Peterson, and S. Masuzaki. 3d effects of edge magnetic field configuration on divertor/scrape-off layer transport and optimization possibilities for a future reactor. *Nuclear Fusion*, 55(10):104021, 2015.

[50] A.S. Kukushkin, H.D. Pacher, A. Loarte, V. Komarov, V. Kotov, M. Merola, G.W. Pacher, and D. Reiter. Analysis of performance of the optimized divertor in ITER. *Nuclear Fusion*, 49(7):075008, 2009.

[51] R.Schneider, H. Renner, X. Bonnin, D. Coster, and J. Neuhauser. Divertor for W7-X: II. comparison of island and axisymmetric divertor. *Plasma Physics and Controlled Fusion*, 44(6):665, 2002.

[52] Y Feng, M Kobayashi, T Lunt, and D Reiter. Comparison between stellarator and tokamak divertor transport. *Plasma Physics and Controlled Fusion*, 53(2):024009, 2011.

[53] K.J. Brunner, T. Akiyama, M. Hirsch, J. Knauer, P. Kornejew, B. Kursinski, H. Laqua, J. Meineke, H. Trimiño Mora, and R. C. Wolf. Real-time dispersion interferometry for density feedback in fusion devices. *Journal of Instrumentation*, 13(09):P09002–P09002, sep 2018.

[54] Tom Wauters, Andrei Goriaev, Arturo Alonso, Juergen Baldzuhn, Rudolf Brakel, Sebastijan Brezinsek, Andreas Dinklage, Heinz Grote, Joris Fellinger, Oliver P. Ford, Ralf König, Heinrich Laqua, Dmitry Matveev, Torsten Stange, and Lilla Vanó. Wall conditioning throughout the first carbon divertor campaign on Wendelstein 7-X. *Nuclear Materials and Energy*, 17:235 – 241, 2018.

[55] D. Zhang, R. Burhenn, R. Koenig, L. Giannone, P. A. Grodzki, B. Klein, K. Grosser, J. Baldzuhn, K. Ewert, V. Erckmann, M. Hirsch, H. P. Laqua, and J. W. Oosterbeek. Design criteria of the bolometer diagnostic for steady-state operation of the W7-X stellarator. *Review of Scientific Instruments*, 81(10):10E134, 2010.

[56] D. H. Lehmer. On the compounding of certain means. *J. Math. Anal. Appl.*, 36:183–200, 1971.

[57] Y Feng, F Sardei, P Grigull, K McCormick, J Kisslinger, D Reiter, and Y Igitkhanov. Transport in island divertors: physics, 3D modelling and comparison to first experiments on W7-AS. *Plasma Physics and Controlled Fusion*, 44(5):611, 2002.

[58] Y. Feng, H. Frerichs, M. Kobayashi, A. Bader, F. Effenberg, D. Harting, H. Hoelbe, J. Huang, G. Kawamura, J. D. Lore, T. Lunt, D. Reiter, O. Schmitz, and D. Sharma. Recent Improvements in the EMC3-Eirene Code. *Contributions to Plasma Physics*, 54(4-6):426–431, 2014.

[59] U. Wenzel, T. Kremeyer, G. Schlisio, M. Marquardt, T.S. Pedersen, O. Schmitz, B. Mackie, and J. Maisano-Brown and. Advanced neutral gas diagnostics for magnetic confinement devices. *Journal of Instrumentation*, 12(09):C09008–C09008, sep 2017.

[60] A.A. Pshenov, A.S. Kukushkin, and S.I. Krasheninnikov. Energy balance in plasma detachment. *Nuclear Materials and Energy*, 12:948 – 952, 2017.

[61] H.Y. Guo, D.N. Hill, A.W. Leonard, S.L. Allen, P.C. Stangeby, D. Thomas, E.A. Unterberg, T. Abrams, J. Boedo, A.R. Briesemeister, D. Buchenauer, I. Bykov, J.M. Canik, C. Chrobak, B. Covele, R. Ding, R. Doerner, D. Donovan, H. Du, D. Elder, D. Eldon, A. Lasa, M. Groth, J. Guterl, A. Jarvinen, E. Hinson, E. Kolemen, C.J. Lasnier, J. Lore, M.A. Makowski, A. McLean, B. Meyer, A.L. Moser, R. Nygren, L. Owen, T.W. Petrie, G.D. Porter, T.D. Rognlien, D. Rudakov, C.F. Sang, C. Samuell, H. Si, O. Schmitz, A. Sontag, V. Soukhanovskii, W. Wampler, H. Wang, and J.G. Watkins. Developing and validating advanced divertor solutions on DIII-d for next-step fusion devices. *Nuclear Fusion*, 56(12):126010, sep 2016.

[62] Ph. Mertens and B. Brezinsek. Recycling of hydrogen isotopes - from an identification of mechanisms in textor to a wider formulation. *Fusion Science and Technology*, 47(2):161–171, 2005.

[63] S Brezinsek, G Sergienko, A Pospieszczyk, Ph Mertens, U Samm, and P T Greenland. Characterization of the deuterium recycling flux in front of a graphite surface in the TEXTOR tokamak. *Plasma Physics and Controlled Fusion*, 47(4):615–634, mar 2005.

[64] S. Brezinsek, A. Pospieszczyk, D. Borodin, M.F. Stamp, R. Pugno, A.G. McLean, U. Fantz, A. Manhard, A. Kallenbach, N.H. Brooks, M. Groth, Ph. Mertens, V. Philipps, and U. Samm. Hydrocarbon injection for quantification of chemical erosion yields in tokamaks. *Journal of Nuclear Materials*, 363–365(0):1119 – 1128, 2007.

[65] M.F.A. Harrison et al. *Atomic Collision Physics*, volume 2. Academic Press, 1984.

[66] F. Effenberg, S. Brezinsek, Y. Feng, M. Jakubowski, R. Koenig, M. Krychowiak, H. Niemann, V. Perseo, O. Schmitz, D. Zhang, A. Ali, T. Barbui, C. Biedermann, R. Burhenn, B. Buttenschoen, P. Drewelow, H. Frerichs, Y. Gao, J. Geiger, C. Killer, D. Grdic, G Kocsis, M. Otte, A. Puig Sitjes, F. Reimold, L. Rudischhauser, T. Sunn Pedersen, Y. Suzuki, T. Szepesi, V. Winters, and G.A. Wurden and the W7-X team. Demonstration of power exhaust control by impurity seeding at Wendelsetin 7-X. 2018. Fusion Energy Conference of the IAEA, Mahatma Mandir, India - contributed oral presentation.

[67] F. Effenberg, S. Brezinsek, Y. Feng, R. König, M. Krychowiak, M. Jakubowski, H. Niemann, V. Perseo, O. Schmitz, D. Zhang, T. Barbui, C. Biedermann, R. Burhenn, B. Buttenschön, G. Kocsis, A. Pavone, F. Reimold, T. Szepesi, H. Frerichs, Y. Gao, U. Hergenhahn, S. Kwak, M. Otte, and T. Sunn Pedersen and. First demonstration of radiative power exhaust with impurity seeding in the island divertor at Wendelstein 7-X. *Nuclear Fusion*, 59(10):106020, aug 2019.

[68] Ralf König, J. Baldzuhn, W. Biel, C. Biedermann, H.S. Bosch, S. Bozhenkov, T. Bräuer, B. Brotas de Carvalho, R. Burhenn, B. Buttenschön, G. Cseh, A. Czarnecka, M. Endler, V. Erckmann, T. Estrada, J. Geiger, O. Grulke, D. Hartmann, D. Hathiramani, M. Hirsch, S. Jabłonski, M. Jakubowski, J. Kaczmarczyk, T. Klinger, S. Klose, G. Kocsis, P. Kornejew, A. Krämer-Flecken, T. Kremeyer, M. Krychowiak, M. Kubkowska, A. Langenberg, H. P. Laqua, M. Laux, Y. Liang, A. Lorenz, A.O. Marchuk, V. Moncada, O. Neubauer, U. Neuner, J.W. Oosterbeek, M. Otte, N. Pablant, E. Pasch, T.S. Pedersen, K. Rahbarnia, L. Ryc, O. Schmitz, W. Schneider, H. Schuhmacher, B. Schweer, T. Stange, H. Thomsen, J.-M. Travere, T. Szepesi, U. Wenzel, A. Werner, B. Wiegel, T. Windisch, R. Wolf, G.A. Wurden, D. Zhang, A. Zimbal, S. Zoletnik, and the W7-X Team. The Set of Diagnostics for the First Operation Campaign of the Wendelstein 7-X Stellarator. *Journal of Instrumentation*, 10(10):P10002, 2015.

[69] T. Barbui, S.A. Bozhenkov, F. Effenberg, C. Favreau, E. Flom, G. Fuchert, P. Drews, K. Hammond, M. Jakubowski, C. Killer, R. König, M. Krychowiak, S. Loch, J. Muñoz Burgosd, E. Pasch, O. Schmitz, E.R. Scott, M. Vecsei, S. Zoletnik, and the W7-X Team. The He/Ne beam diagnostic for line-ratio spectroscopy in the island divertor of Wendelstein 7-X. *Journal of Instrumentation*, 14:C07014, 2019.

[70] T. Barbui, M. Krychowiak, R. König, O. Schmitz, J. M. Muñoz Burgos, B. Schweer, and A. Terra. Feasibility of line-ratio spectroscopy on helium and neon as edge diagnostic tool for Wendelstein 7-X. *Review of Scientific Instruments*, 87(11):11E554, 2016.

[71] M. Krychowiak, A. Adnan, A. Alonso, T. Andreeva, J. Baldzuhn, T. Barbui, M. Beurskens, W. Biel, C. Biedermann, B. D. Blackwell, H. S. Bosch, S. Bozhenkov, R. Brakel, T. Bräuer, B. Brotas de Carvalho, R. Burhenn, B. Buttenschön, A. Cappa, G. Cseh, A. Czarnecka, A. Dinklage, P. Drews, A. Dzikowicka, F. Effenberg, M. Endler, V. Erckmann, T. Estrada, O. Ford, T. Fornal, H. Frerichs, G. Fuchert, J. Geiger, O. Grulke, J. H. Harris, H. J. Hartfuß, D. Hartmann, D. Hathiramani, M. Hirsch, U. Höfel, S. Jabłoński, M. W. Jakubowski, J. Kaczmarczyk, T. Klinger, S. Klose, J. Knauer, G. Kocsis, R. König, P. Kornejew, A. Krämer-Flecken, N. Krawczyk, T. Kremeyer, I. Ksiazek, M. Kubkowska, A. Langenberg, H. P. Laqua, M. Laux, S. Lazerson, Y. Liang, S. C. Liu, A. Lorenz, A. O. Marchuk, S. Marsen, V. Moncada, D. Naujoks, H. Neilson, O. Neubauer, U. Neuner, H. Niemann, J. W. Oosterbeek, M. Otte, N. Pablant, E. Pasch, T. Sunn Pedersen, F. Pisano, K. Rahbarnia, L. Ryć, O. Schmitz, S. Schmuck, W. Schneider, T. Schröder, H. Schuhmacher, B. Schweer, B. Standley, T. Stange, L. Stephey, J. Svensson, T. Szabolics, T. Szepesi, H. Thomsen, J.-M. Travere, H. Trimino Mora, H. Tsuchiya, G. M. Weir, U. Wenzel, A. Werner, B. Wiegel, T. Windisch, R. Wolf, G. A. Wurden, D. Zhang, A. Zimbal, S. Zoletnik, and W7-X Team. Overview of diagnostic performance and results for the first operation phase in Wendelstein 7-X (invited). *Review of Scientific Instruments*, 87(11):11D304, 2016.

[72] O Schmitz, I L Beigman, L A Vainshtein, B Schweer, M Kantor, A Pospieszczyk, Y Xu, M Krychowiak, M Lehnen, U Samm, B Unterberg, and the TEXTOR team. Status of electron temperature and density measurement with beam emission spectroscopy on thermal helium at TEXTOR. *Plasma Physics and Controlled Fusion*, 50(11):115004, 2008.

[73] E. Pasch, M. N. A. Beurskens, S. A. Bozhenkov, G. Fuchert, J. Knauer, and R. C. Wolf. The Thomson scattering system at Wendelstein 7-X. *Review of Scientific Instruments*, 87(11):11E729, 2016.

[74] S.A. Bozhenkov, M. Beurskens, A. Dal Molin, G. Fuchert, E. Pasch, M.R. Stoneking, M. Hirsch, U. Höfel, J. Knauer, J. Svensson, H. Trimino Mora, and R.C. Wolf. The Thomson scattering diagnostic at Wendelstein 7-X and its performance in the first operation phase. *Journal of Instrumentation*, 12(10):P10004–P10004, oct 2017.

[75] Tullio Barbui, Maciej Krychowiak, Oliver Schmitz, Sergey A Bozhenkov, Erik Flom, Golo Fuchert, Carsten Killer, Ralf König, Marcin Jakubowski, Jorge Manuel Munoz Burgos, Ekkehard Pasch, and Evan R Scott. Measurements of plasma parameters in the divertor island of Wendelstein 7-X through line-ratio spectroscopy on helium. *Nuclear Fusion*, at press, 2020.

[76] D. Zhang, R. König, Y. Feng, R. Burhenn, S. Brezinsek, M. Jakubowski, B. Buttenschön, H. Niemann, A. Pavone, M. Krychowiak, S. Kwak, J. Svensson, Y. Gao, T. S. Pedersen, A. Alonso, J. Baldzuhn, C. D. Beidler, C. Biedermann, S. Bozhenkov, K. J. Brunner, H. Damm, M. Hirsch, L. Giannone, P. Drewelow, F. Effenberg, G. Fuchert, K. C. Hammond, U. Höfel, C. Killer, J. Knauer, H. P. Laqua, R. Laube, N. Pablant, E. Pasch, F. Penzel, K. Rahbarnia, F. Reimold, H. Thomsen, V. Winters, F. Wagner, T. Klinger, and W7-X team. First Observation of a Stable Highly Dissipative Divertor Plasma Regime on the Wendelstein 7-X Stellarator. *Phys. Rev. Lett.*, 123:025002, Jul 2019.

[77] M. Kobayashi, S. Morita, C.F. Dong, Z.Y. Cui, Y.D. Pan, Y.D. Gao, H.Y. Zhou, Y. Feng, S. Masuzaki, M. Goto, T. Morisaki, H. Yamada, J. Cheng, P. Sun, Q.W. Yang, X.R. Duan, and the LHD Experiment Group. Edge impurity transport study in the stochastic layer of LHD and the scrape-off layer of HL-2A. *Nuclear Fusion*, 53(3):033011, 2013.

[78] M. Kobayashi, S. Masuzaki, I. Yamada, Y. Narushima, C. Suzuki, N. Tamura, B.J. Peterson, S. Morita, C.F. Dong, N. Ohno, S. Yoshimura, Y. Feng, M. Goto, K. Sato, T. Akiyama, K. Tanaka, and the LHD experiment group. Control of 3D edge radiation structure with resonant magnetic perturbation fields applied to the stochastic layer and stabilization of radiative divertor plasma in LHD. *Nuclear Fusion*, 53(9):093032, 2013.

[79] Yong-Ki Kim and Jean-Paul Desclaux. Ionization of carbon, nitrogen, and oxygen by electron impact. *Phys. Rev. A*, 66:012708, Jul 2002.

[80] R.R. Weynants, A.M. Messiaen, J. Ongena, B. Unterberg, G. Bonheure, P. Dumortier, R. Jaspers, R. Koch, H.R. Koslowski, A. Krämer-Flecken, G. Mank, J. Rapp, M.Z. Tokar', G. Van Wassenhove, W. Biel, M. Brix, F. Durodié, G. Esser, K.H. Finken, G. Fuchs, B. Giesen, J. Hobirk, P. Hüttemann, M. Lehnen, A. Lyssoivan, P. Mertens, A. Pospieszczyk, U. Samm, M. Sauer, B. Schweer, R. Uhlemann, G. Van Oost, P.E. Vandenplas, M. Vervier, V. Philipps, G. Waidmann, and G.H. Wolf. Overview of radiative improved mode results on TEXTOR-94. *Nuclear Fusion*, 39(11Y):1637, 1999.

[81] E.A. Unterberg, O. Schmitz, T.E. Evans, R. Maingi, N.H. Brooks, M.E. Fenstermacher, S. Mordijck, R.A. Moyer, and D.M. Orlov. The effects of an open and closed divertor on particle exhaust during edge-localized mode suppression by resonant magnetic perturbations in DIII-D. *Nuclear Fusion*, 50(3):034011, 2010.

[82] O. Schmitz, J.W. Coenen, H. Frerichs, M. Kantor, M. Lehnen, B. Unterberg, S. Brezinsek, M. Clever, T. Evans, K.H. Finken, M. Jakubowski, A. Kraemer-Flecken, V. Phillips, D. Reiter, U. Samm, G.W. Spakman, and G. Telesca. Particle confinement control with resonant magnetic perturbations at TEXTOR. *Journal of Nuclear Materials*, 390 - 391(0):330 – 334, 2009.

[83] Thierry Kremeyer. *Particle Fueling and Exhaust in the W7-X Island Divertor*. PhD thesis, University of Wisconsin - Madison, https://search.library.wisc.edu/catalog/9912906971102121, December 2019.

[84] Victoria Winters. *Impurity Transport in the W7-X Island Divertor*. PhD thesis, University of Wisconsin - Madison, https://search.library.wisc.edu/catalog/9912848087502121, July 2019.

[85] A. W. Leonard, G. D. Porter, R. D. Wood, S. L. Allen, J. Boedo, N. H. Brooks, T. E. Evans, M. E. Fenstermacher, D. N. Hill, R. C. Isler, C. J. Lasnier, R. D. Lehmer, M. A. Mahdavi, R. Maingi, R. A. Moyer, T. W. Petrie, M. J. Schaffer, M. R. Wade, J. G. Watkins, W. P. West, and D. G. Whyte. Radiative divertor plasmas with convection in diii-d. *Physics of Plasmas*, 5(5):1736–1743, 1998.

[86] J. Rapp, A. Kallenbach, R. Neu, T. Eich, R. Fischer, A. Herrmann, S. Potzel, G.J. van Rooij, and J.J. Zielinski and. Radiative type-III ELMy h-mode in all-tungsten ASDEX upgrade. *Nuclear Fusion*, 52(12):122002, nov 2012.

[87] F. Reimold, M. Wischmeier, M. Bernert, S. Potzel, A. Kallenbach, H.W. Müller, B. Sieglin, and U. Stroth and. Divertor studies in nitrogen induced completely detached h-modes in full tungsten ASDEX upgrade. *Nuclear Fusion*, 55(3):033004, feb 2015.

[88] T. Morisaki, K. Oyama, N. Tamura, S. Masuzaki, T. Akiyama, G. Motojima, J. Miyazawa, B.J. Peterson, N. Ohno, and H. Yamada. Radiated power distributions in impurity-seeded plasmas in lhd. *Journal of Nuclear Materials*, 463:640 – 643, 2015. PLASMA-SURFACE INTERACTIONS 21.